

Microalgae-based Intestinal villi-targeting multistage biosystem for irritable bowel syndrome treatment

Received: 19 November 2024

Accepted: 21 July 2025

Published online: 15 August 2025

Jiahui Ye^{1,2,3,4}, Haimeng Sun^{3,4}, Qing Zhang^{3,4}, Jian He^{1,2,3,4} & Min Zhou^{1,2,3,4} 

Irritable Bowel Syndrome (IBS) is a chronic gastrointestinal disorder associated with dysregulation of the gut-brain axis. Current treatment approaches often lack long-term efficacy and target specificity, and there are no drugs or formulations specifically targeting this disease. Owing to chronic and intermittent gastrointestinal motility disturbances, the pharmacokinetic parameters of IBS patients change significantly. In this research, we develop an oral engineered microalgae biosystem by integrating microalgae with myricetin nanoparticles to enhance the treatment of IBS. After cultivation and micro-nano transformation, the engineered microalgae can be captured by intestinal villi and remain attached. The nano-coating further enhances the adhesion to intestinal tissue and resistance to gastric acid. This biosystem aims to address the pharmacokinetic complications in IBS that are not resolvable by enteric-coated capsules. Interestingly, microalgae seem to exert their prebiotic potential, assisting myricetin in increasing short-chain fatty acids levels and further regulating IBS multi-organ symptoms through the gut-brain axis.

Irritable bowel syndrome (IBS) is a complex gastrointestinal disorder that affects ~10–15% of the global population^{1,2}. It is characterized by abdominal pain, bloating, and alterations in bowel habits, significantly impacting the quality of life of patients and may encompass systemic manifestations involving the nervous and digestive systems^{3,4}. The symptoms of IBS are multifaceted, including intestinal motility disorders, visceral hypersensitivity⁵, and dysregulation of the microbiota-gut-brain axis^{6,7}. Current therapeutic approaches, such as antispasmodics⁸, probiotics⁹, neuromodulators, and dietary modifications^{10,11}, are poorly specific and often offer limited relief, and may give rise to adverse reactions⁴. Moreover, the development of drugs and formulations for IBS is scarce compared to that of other diseases¹².

Diseases such as diarrhea-predominant IBS (IBS-D) pose unique challenges for oral drug delivery due to significant dynamics and microenvironment alterations in the intestinal tract, including compromised epithelial integrity, modified mucus layer, and accelerated transit time^{13,14}. Such physiological variations significantly influence the

pharmacokinetics of oral drugs, compromising their absorption, distribution, and bioavailability, which could be a key underlying factor contributing to the poor reproducibility in IBS-D research and clinical trials¹⁵. At this point, employing higher doses to achieve therapeutic efficacy may amplify side effects and reduces patient compliance. Distinct from common diarrhea, the manifestation of symptoms in IBS-D is chronic and unpredictable¹³, which cautions us against disregarding this particularity and directly adopting some generalized dosage forms. Nowadays, numerous research efforts have concentrated on formulating advanced drug delivery system¹⁶. However, relevant works specifically targeting IBS-D are extremely rare, and clinical options are highly limited. Further research on innovative and reliable drug delivery mechanisms is imperative.

Myricetin (MY), a plant-derived flavonoid, can mitigate intestinal inflammation and barrier dysfunction due to its anti-inflammatory and antioxidant properties¹⁷. Studies have indicated that MY can inhibit mast cell degranulation and the release of cytokines, presenting a favorable application prospect for the treatment of allergic

¹Eye Center, The Second Affiliated Hospital, Zhejiang University School of Medicine, Hangzhou, P. R. China. ²Institute of Translational Medicine, Zhejiang University, Hangzhou, P. R. China. ³Zhejiang University-University of Edinburgh Institute (ZJU-UoE Institute), Zhejiang University, Haining, P. R. China. ⁴Zhejiang University-Erdos Etuoke Joint Research Center, The Second Affiliated Hospital, Zhejiang University, Hangzhou, P. R. China. ✉e-mail: zhoum@zju.edu.cn

diseases^{18,19}. Numerous studies have demonstrated that in IBS-D, mast cell activation and its interaction with the enteric nervous system (ENS) significantly contribute to visceral hypersensitivity^{20–22}. Consequently, the pharmacological activity of MY has shown potential in alleviating IBS-D symptoms. Nevertheless, its clinical application is hampered by low solubility, rapid degradation in the gastrointestinal environment, and insufficient targeted delivery²³.

Therefore, a delivery system suitable for IBS-D should, first and foremost, be capable of maintaining the stability of patients' pharmacokinetics, that is, not being interfered with in drug distribution by the dysfunctional intestine. Secondly, it is necessary to find means to enhance the bioavailability of potential drugs. Additionally, in IBS-D, factors such as the close association between the intestinal microbiota and symptoms, the persistent mental symptoms of patients, and the presence of small intestinal bacterial overgrowth (SIBO) in some patients should all be taken into account as much as possible²⁴. *Spirulina* (SP) is a microalga with a distinctive spiral morphology, and its diameter is slightly smaller than the spacing between intestinal villi, facilitating its capture by the villi for long-term retention²⁵. Due to this characteristic, it holds considerable potential as a drug delivery carrier of oral administration²⁶. As a microorganism, it is mass-produced and developed into dietary supplements because it is rich in various nutrients^{27,28}, and numerous studies have indicated its ability to regulate the intestinal microbiota^{29,30}.

This study proposes an effective oral engineered microalgae-nano biosystem (SP@MYnn) based on microalgae. SP@MYnn is capable of resolving the abnormal pharmacokinetics of IBS-D that clinical enteric-coated capsules are unable to cope with. The antibacterial nano-coating with viscous properties is used to attach MY nanoparticles onto SP, which further enhances the adhesion of SP to intestinal tissues and resistance to dysmotility. In addition, the nanoparticles improve the solubility and bioavailability of MY, resist acid in the stomach, and have the potential to resist SIBO. Furthermore, SP fully utilizes its prebiotic potential, enriching beneficial bacterial genera such as *Lactobacillus*, increasing beneficial short-chain fatty acids (SCFAs) such as butyric acid, and reducing isovaleric acid, a potentially harmful bacterial metabolite. To sum up, engineered microalgae accomplish multi-organ and multi-symptom therapy against anti-diarrhea, suppression of visceral hypersensitivity, and modulation of the brain-gut axis.

Results

Gastrointestinal motility disorders in IBS-D and design schemes of engineered microalgae

Firstly, we selected the available expression profile dataset (GSE36701) from NCBI. The intestinal tissues of three groups, namely IBS-D, PIBD (IBS patients post *Campylobacter jejuni* infection) and PIBS (IBS patients post undefined infection), were respectively compared with those of healthy volunteers (HV) to screen for differentially expressed genes. A relatively more differentially expressed genes were screened out in PIBS patients, and the upregulation of inflammation-related genes was evident, which was more inclined towards enteritis rather than IBS. We speculate that this is because the unknown pathogen leads to significant heterogeneity among patients, and thus the reference significance is limited (Supplementary Fig. 1). When comparing the IBS-D and PIBD groups with HV, it was discovered that genes such as vasoactive intestinal peptide (VIP), which may lead to excessive intestinal peristalsis and secretion, as well as genes like IL-33 that directly activate mast cells, were upregulated (Supplementary Fig. 2). Interestingly, after conducting Kyoto Encyclopedia of Genes and Genomes (KEGG) functional enrichment, the differential genes of the PIBD group were related to neuroactive ligand-receptor interaction, circadian rhythm, vascular smooth muscle contraction, calcium signaling pathway, etc., while the differential genes of the IBS-D group were enriched in GABAergic synapse, glutamatergic synapse, bile secretion, adrenergic signaling in cardiomyocytes, cortisol synthesis

and secretion (Fig. 1a–b). These pathways are primarily related to intestinal motility disorders and visceral pain^{31,32}. Subsequently, we measured the pharmacokinetics of MY and MY encapsulated in enteric-coated capsules (MY@Cap). In the IBS-D model, the peak plasma concentration (C max) of MY was decreased, the time to reach peak concentration (T max) was prolonged, and the bioavailability was significantly reduced. Even more crucially, the ability of MY@Cap to maintain stable blood drug concentrations and achieve long-term sustained release was also significantly impacted (Fig. 1c–e). Fluorescein isothiocyanate (FITC) was used to encapsulate FITC@Cap instead of MY and it was found that IBS-D resulted in the rapid elimination of both FITC and FITC@Cap (Fig. 1f). The above results all indicate that the commonly used sustained-release capsules in clinical practice cannot fulfill the requirements of IBS-D. Subsequently, scanning electron microscopy (SEM) reveals the status of SP in the small intestine. The elongated structure is deeply lodged in the interstices of the villi, presenting the potential to resist excessive intestinal motility and excessive secretion in IBS-D (Fig. 1g and Supplementary Fig. 3). Subsequently, as stated in the Introduction, we constructed engineered microalgae and investigated whether it could meet the therapeutic requirements for IBS-D. Briefly, the poorly soluble MY was encapsulated in poly (lactic-co-glycolic acid) (MY@PLGA) by ultrasonic emulsification, followed by encapsulation in a viscous and anti-bacterial quaternary ammonium chitosan (CS) layer (MYnano), and subsequently coated on the surface of SP cells (Fig. 1h).

Synthesis and characterization

MYnano significantly enhances the solubility and dispersibility of MY, presenting as spherical particles with a diameter of around 300 nm (Fig. 2a–c). MYnano is rapidly and uniformly assembled on the large surface area of SP (Fig. 2d–e and Supplementary Fig. 4–5). The UV-visible spectroscopy reveals that SP@MYnn simultaneously possesses the characteristic absorption peaks of both MYnano and SP. Moreover, after assembly, the surface charge of SP turns from negative to positive (Fig. 2f–g). The intense chlorophyll fluorescence of SP@MYnn not only endows it with the potential to be an imaging biomaterial but also suggests that the active substances in SP are maintained after assembly²⁶, thereby laying the groundwork for its prebiotic potential. We labeled MYnano with DiO, and through 3D scanning, discovered that the diameter of SP was about 3,779 nm, while the diameter of the nano-coating reached about 11,973 nm, demonstrating the strong drug-loading capacity of biosystem (Fig. 2h). Additionally, the degradation rate of SP@MYnn in artificial simulated gastric fluid (SGF) was significantly lower than that in artificial simulated small intestinal fluid (SIF) and colonic fluid (SCF), indicating that it can protect MY and SP in the harsh gastric environment (Fig. 2i). Unlike commercial reagents, the lengths and growth states of SP exhibit significant individual variations, and we also observed the same phenomenon on SP with longer lengths and more pronounced spiral structures (Fig. 2j and Supplementary Fig. 6). In the subsequent experiments, we ascertained that when the reaction time was 60 min and the mass ratio of SP to MY was 5:1, the conditions for best reaction encapsulation efficiency (EE) were met (Supplementary Fig. 7). Then, we simulated the entire release process of SP@MY at different times *in vitro*. To put it simply, the change was negligible in SGF, while a gradual release occurred in the intestinal fluid and the surface of SP was exposed. There is no significant difference was observed in the drug release of SP@MYnn and MYnano in SGF (Fig. 2k and Supplementary Figs. 8–9).

In vivo distribution as well as adhesion and anti-SIBO characteristics

The intestinal contents were collected for SEM observation and the release kinetics of SP@MYnn *in vivo* were similar to those in the *in vitro* experiments (Fig. 3a and Supplementary Fig. 10). Then, MYnano labeled with DiO was used to synthesize SP@MYnn, so fluorescence

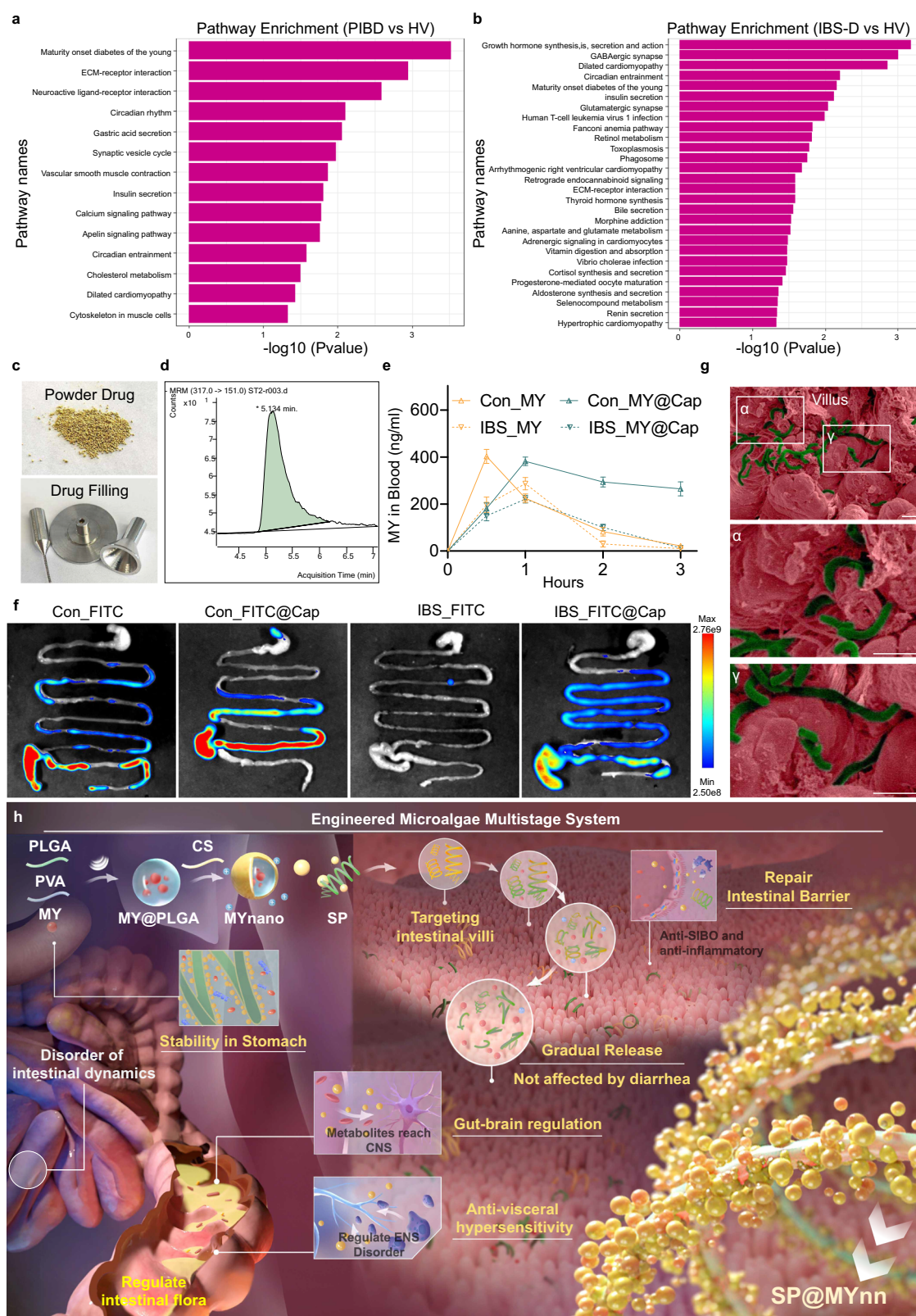


Fig. 1 | IBS-D induces intestinal motility disorders and disturbances in drug absorption. **a, b** Functional enrichment of KEGG pathways for the differentially expressed genes in the PIBD group (a) and the IBS-D group (b). Modified t-test of the limma package (which combines empirical Bayesian variance adjustment) was used for comparisons between two groups. **c** MY Powder and MY@Cap preparation. **d** Representative MRM mass spectrometry chromatogram of MY. **e** Blood MY concentration in each group ($n = 3$ biologically independent animals). **f** Ex vivo

distribution of FITC fluorescence in each group at 4 h after gavage. **g** SEM (pseudo-color) of gut after taking oral SP, scale bar = 20 μm . **h** Schematic illustration of engineered microalgae multistage biosystem. The data show means + SD. *PLGA* poly(lactic-co-glycolic acid); *PVA* polyvinyl alcohol; *MY* myricetin; *CS* chitosan; *SP* spirulina platensis; *SIBO* small intestinal bacterial overgrowth. Source data are provided as a Source Data file.

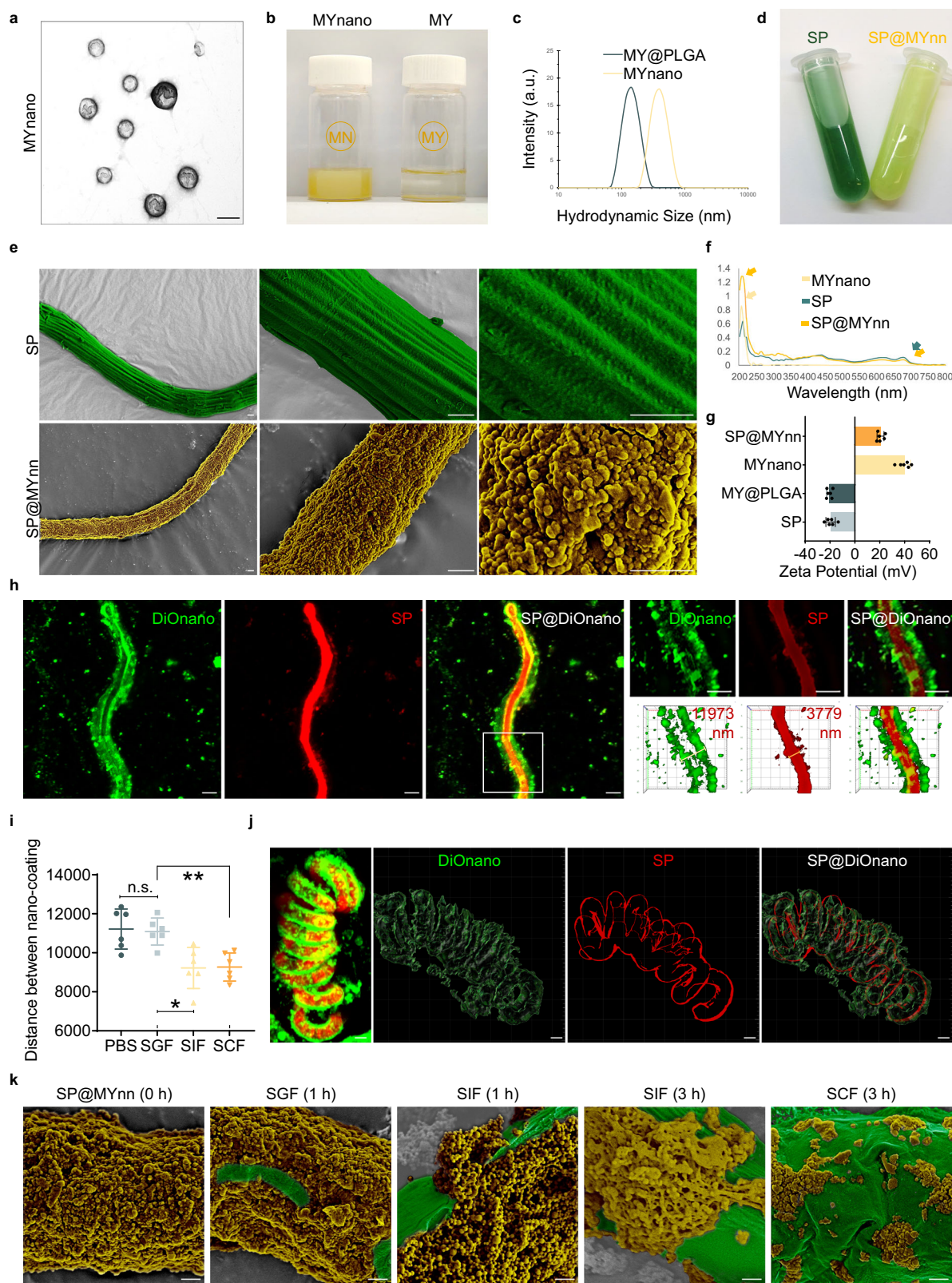
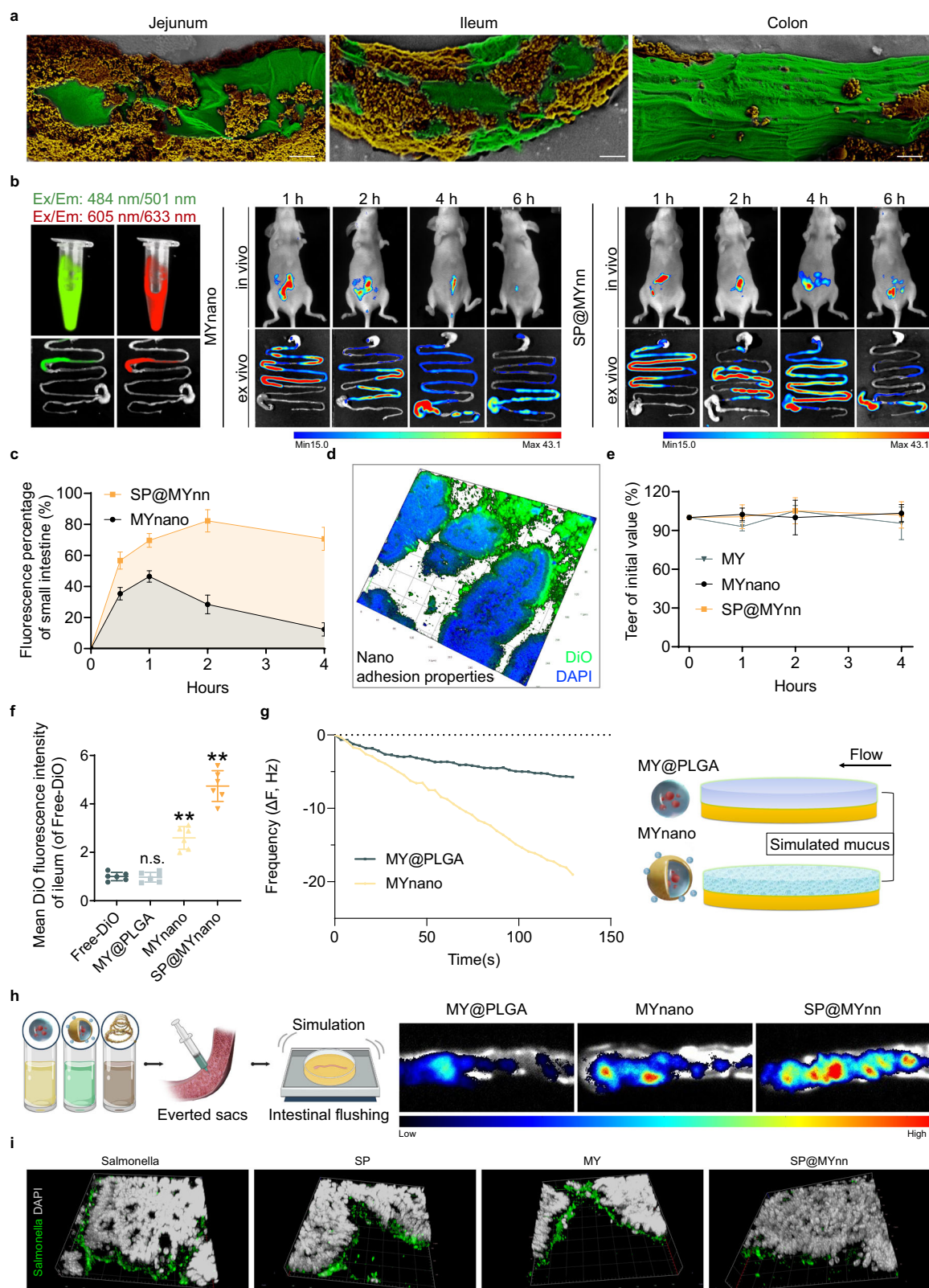


Fig. 2 | Synthesis and characterization of engineered microalgae biosystem. **a** TEM image of MYnano, scale bar = 300 nm. **b** Dissolution of MYnano and MY. **c** Hydrodynamic size distribution of MY@PLGA and MYnano. **d–e** SP and SP@MYnn (**d**), along with their SEM images (pseudo-color) (**e**), scale bar = 1 μ m. **f** UV-visible spectrum. **g** Zeta potential ($n = 6$ independent experiments). **h** Fluorescence and 3D images of SP@DiOnano (DiO-labeled SP@MYnn), scale bar = 10 μ m. **i** Diameter of the DiO-nano coating ($n = 6$ independent experiments). One-

way ANOVA with Tukey's post hoc test was used for comparisons among multiple groups, SGF vs. PBS, $P = 0.9945$; SIF vs. SGF, $P = 0.0082$; SCF vs. SGF, $P = 0.0102$. **j** Another fluorescence images of SP@DiOnano under different growth conditions and 3D reconstruction, scale bar = 5 μ m. **k** SEM images (pseudo-color) of SP@MYnn after treatment with SGF, SIF, or SCF, scale bar = 600 nm. The data show means + SD (* < 0.05, ** < 0.01, n.s., no significance). Source data are provided as a Source Data file.



could be excited in both the red channel for SP and the green channel for DiO. After biosystem gavage, the locations of both were the same, further indicating the close combination of MYnano (green) and SP (red). The DiO channel is more appropriate for detecting the distribution of drugs, and the fluorescence in vivo and ex vivo suggests that the assembly of SP significantly prolongs the intestinal retention time of MY. Besides, the distribution of the drug in the intestine

becomes more widespread, which is associated with the villus-targeting property of SP (Fig. 3b–c). Subsequently, the strong adhesion of MYnano to intestinal tissue was observed via frozen section. Since DiO is a commonly employed cell membrane dye, we co-incubated DiO-labeled MYnano and MY@PLGA with intestinal epithelial cells (IEC-6), and the MYnano group demonstrated stronger cell membrane luminance. Intestinal tissue also presented a similar

Fig. 3 | In vivo distribution, drug release and surface characteristics. **a** SEM images (pseudo-color) of intestinal contents, scale bar = 1 μ m. **b** SP@MYnn's in vivo and ex vivo fluorescence images. **c** Percentage of small intestine DiO fluorescence area ($n = 6$ biologically independent animals). **d** Fluorescence images of ileum after biosystem oral administration. **e** Teer of the IEC-6 monolayer cell model after co-cubation with biosystem ($n = 3$ biologically independent cells). **f** Fluorescence intensity of the ileum at 4 h after oral administration of free DiO and DiO-labeled materials ($n = 6$ biologically independent animals). One-way ANOVA with Tukey's

post hoc test was used for comparisons among multiple groups, Free-DiO vs. MY@PLGA, $P = 0.9994$; Free-DiO vs. MYnano, $P < 0.0001$; Free-DiO vs. SP@MYnano, $P < 0.0001$. **g** ΔF of MYnano and MY@PLGA upon introduction into the Mucin coating. Created in BioRender. Ji, C. (<https://BioRender.com/z97wico>). **h** Fluorescence images of everted sacs after oscillation and shaking. Created in BioRender. Ji, C. (<https://BioRender.com/9ujvacd>). **i** Fluorescence images of *Salmonella* in intestine. The data show means + SD (** < 0.01, ## < 0.01, n.s., no significance). Source data are provided as a Source Data file.

tendency. Moreover, through in vitro simulation of the IEC-6 single-layer cell model, the stable trans epithelial electric resistance (Teer) values indicate that the adhesion of MYnano and SP@MYnn will not disrupt the intestinal barrier (Fig. 3d–f and Supplementary Fig. 11). Quartz crystal microbalance (QCM) was employed to further characterize the surface properties in vitro. Mucin was spin-coated on the surface of the chip to simulate the intestinal mucus layer. And then, the suspensions of MY@PLGA and MYnano were introduced into the chamber. As indicated by change of frequency (ΔF), the adhesion amount of the modified MYnano was increased compared with the MY@PLGA (Fig. 3g). Furthermore, we fabricated everted sacs of small intestine, covering their surfaces with equal amounts of MY@PLGA, MYnano, and SP@MYnn. Subsequently, the sacs were subjected to shaking and incubation to simulate intestinal fluid scouring and gastrointestinal motility. It was discovered that the assembly of SP significantly enhanced the distribution of the DiO signal, suggesting that there exists a specific interaction between SP and the villi of the small intestine (Fig. 3h). Finally, regarding the possible concurrent SIBO of IBS-D, with *Salmonella enterica typhimurium SL1344* being taken as a representative, SP@MYnn demonstrated antibacterial capability, and this ability mainly originated from CS³³ (Fig. 3i). To sum up, SP@MYnn demonstrates the properties such as intestinal epithelial adhesion, promotion of drug absorption, and anti-SIBO, which are necessary for the treatment of IBS-D.

SP@MYnn copes with the pharmacokinetic complications of IBS-D

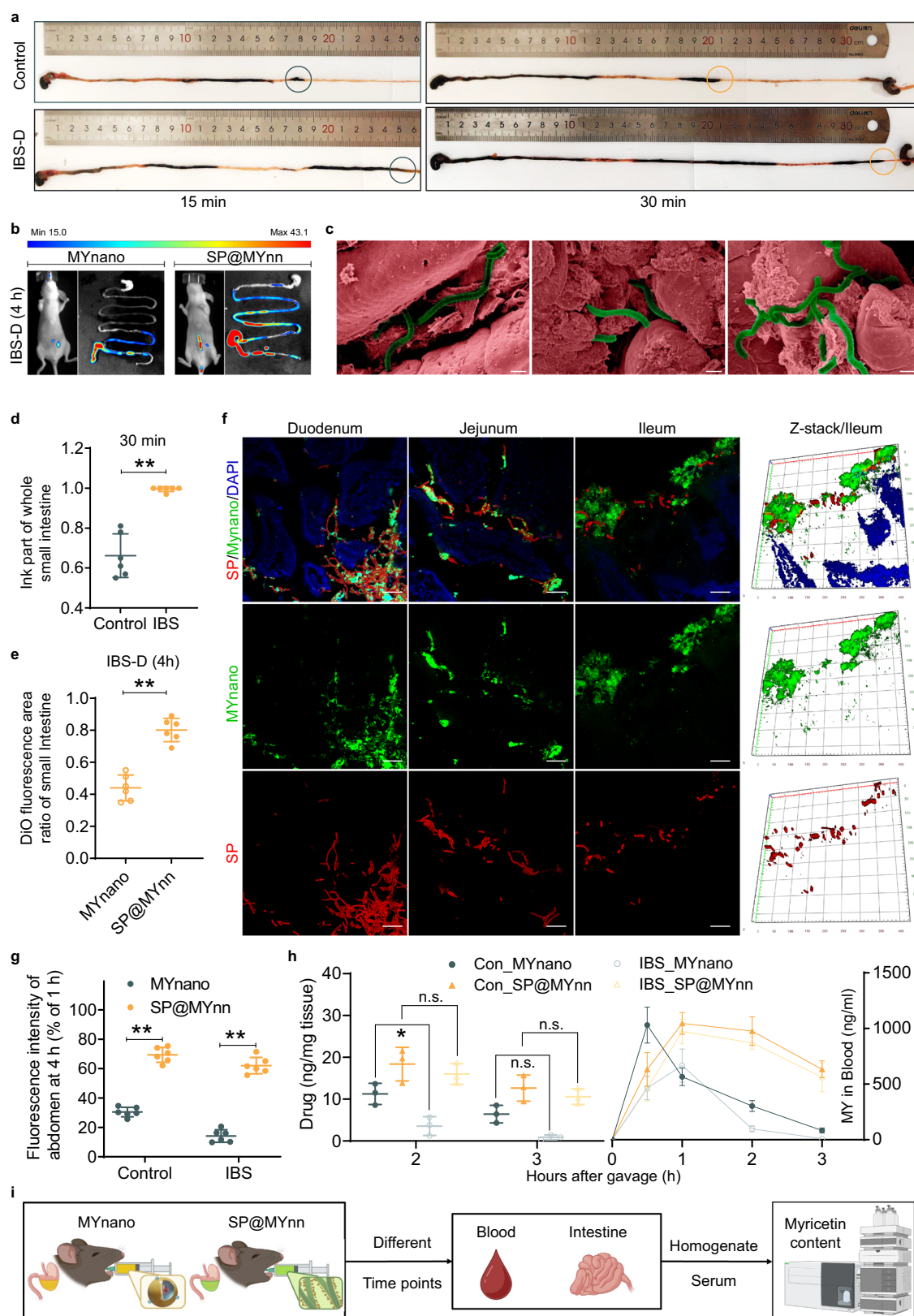
Through intragastric administration of India ink, the ink movement speed in the IBS-D model was faster than that of the control group, showing that the investigated symptoms had emerged (Fig. 4a, d). Similarly, MY@Cap labeled with DiO was fabricated. Subsequently, in vivo imaging demonstrated that in the mice gavaged with SP@MYnn, the drug distribution was not significantly affected by IBS-D, remaining widespread and with a significantly higher fluorescence intensity in the abdomen compared to the MYnano group or the MY@Cap. Observation of SP@MYnn at different positions of the intestine through frozen sections reveals that the co-localization of SP and MYnano is the most extensive in the duodenum and gradually becomes shorter and separated (Fig. 4b, e–g and Supplementary Fig. 12). Moreover, the SEM of intestinal tissue and fluorescence of the contents suggest that in the case of IBS-D, the digestive metabolism of SP and its interaction characteristics with the villi in the small intestine remain unchanged (Fig. 4c and Supplementary Fig. 13). Subsequently, the MY content in the jejunum and blood of mice was detected. It was discovered that MYnano, similar to MY@Cap, was unable to counteract the significant reduction in drug content resulting from IBS-D. In contrast, when SP@MYnn was administered orally, it exhibited similar drug content in both the IBS-D and Control groups, which was consistent with the previous in vivo distribution data (Fig. 4h–i). To sum up, with respect to IBS-D, SP@MYnn demonstrates entirely distinct drug delivery characteristics compared to MYnano and MY@Cap. For the formulations that modify pharmacokinetics, the impacts of their long-term application on key organs and blood biochemical indicators have been habitually evaluated. Generally speaking, no bio-safety concerns have been detected (Supplementary Fig. 14).

Restoration of the intestinal barrier

Clinical IBS-D patients are often accompanied by a history of intestinal infection and symptoms such as mental anxiety and depression¹. To simulate the pathogenesis process of IBS-D to the greatest extent, we infected mice with *Citrobacter rodentium* (CR), and after the elimination of the infection (PI-IBS), combined water avoidance stress (WAS) stimulation to establish the IBS-D model (PI-WA) (Fig. 5a). Through fecal CR counting, CR infection was completely eradicated on the 18th day. During this period, the weight gain of mice slowed down and the defecation rate accelerated (Supplementary Fig. 15). The mucus barrier of the intestine and some tight junction (TJ) proteins are disrupted after IBS-D³⁴, resulting in downstream changes induced by pathogens, toxins, etc. in the intestinal tract. The mucus barrier is mainly maintained by the mucus secreted by goblet cells³⁵. In the PI-WA group, the number of MUC-2-positive goblet cells decreased significantly, and the ability to maintain the mucus barrier declined. Besides, in the PI-WA group, both the ZO-1 and Claudin-1 TJ proteins were downregulated, while occludin remained unchanged. SP@MYnn successfully restored the barrier function, whereas the MY group exhibited unstable and relatively weak repair. In the H&E and AB-PAS staining, the PI-WA group occasionally presented with slight inflammatory pathology in the colon and a decrease in the intestinal mucus layer, which were consistent with the MUC-2 staining (Fig. 5b–g and Supplementary Figs. 16–18). The disruption of the above-mentioned barrier functions led to an increase in the oral permeability of FITC-Dextran, along with an increase in serum lipopolysaccharide (LPS). We successfully established an IBS-D model distinct from inflammatory bowel disease and biosystem restored its intestinal barrier (Fig. 5h–k). Further verification demonstrated that in our PI-WA model, there were no obvious pathological changes in the jejunum and ileum, the inflammatory indicators and the number of inflammatory cells in the colon did not increase, but obvious diarrhea symptoms occurred. And SP@MYnn effectively reduces the quantity of defecation and the water content of feces (Fig. 5l–j and Supplementary Fig. 19).

Regulation of the Intestinal Microenvironment

There exist multiple interaction patterns between the ENS and the immune cells in the intestine, which are closely related to the visceral hypersensitivity and abnormal intestinal motility of IBS-D. We focused on mast cells in particular because numerous studies have reported that there are numerous similarities between IBS-D and allergic reactions³⁶. First of all, in the PI-WA group, the number of colonic mast cells (Tryptase) increased significantly (Supplementary Fig. 20). Subsequently, we selected the areas with dense mast cells in each group to observe their co-localization with intestinal nerve fibers (PGP9.5), and found that PI-WA led to a significant increase in the number of mast cells within 5 μ m of the nerve fibers, suggesting that immune cells were chemotaxing towards the neural tissue. In the PI-WA group, the intestinal protease-activated receptor-2 (PAR-2) was activated by the proteases secreted by mast cells, while simultaneously promoting mast cell degranulation through positive feedback (Fig. 6a–b and Supplementary Fig. 21–22). In the PI-WA group, the abdominal withdrawal reflex (AWR) score increased and the pain threshold decreased, indicating the occurrence of visceral hypersensitivity. Whereas in the SP@MYnn group, engineered microalgae reduced mast cell activation, prevented their chemotaxis towards nerve fibers and inhibited the



activation of the downstream PAR-2 receptor, thereby reducing visceral sensitivity and alleviating the abdominal pain symptoms. Studies have demonstrated that MY possesses the capabilities of anti-allergy¹⁸ and inhibition of mast cell activation, and these capabilities are further strengthened by SP@MYnn (Fig. 6c–d). Similar to the PI-WA group, the pure PI-IBS group also presented similar diarrhea, visceral hypersensitivity, and intestinal barrier damage, which also improved after the

intervention of SP@MYnn (Supplementary Fig. 23). Unlike the decreased weight gain during the period of PI-IBS, no obvious change in weight gain occurred during WAS (Fig. 6e).

The improvement of mental symptoms

In the colon of the PI-WA group, enteric glial cells (EGCs) undergo hyperplasia, which is closely associated with the intestinal stress state.

Fig. 4 | Biosystem copes with intestinal dynamic disorders and drug absorption impairments. **a** Photos of the ink propulsion experiment. **b** In vivo and ex vivo fluorescence images of MYnano and SP@MYnn at 4 h after gavage in IBS-D model. **c** SEM images of the small intestine in SP-treated IBS-D mice, scale bar = 10 μ m. **d** The distance traveled by the ink ($n = 6$ biologically independent animals). Two-tailed unpaired t-tests were used for comparisons between two groups, $P < 0.0001$. **e** DiO fluorescence area ratio of small Intestine at the 4-h time point in IBS-D model (percentage of normal mice) ($n = 6$ biologically independent animals). Two-tailed unpaired t-tests were used for comparisons between two groups, $P < 0.0001$. **f** Frozen section images of the biosystem in intestinal tissue, scale bar = 50 μ m. **g** Fluorescence intensity of abdominal DiO at 4-h time point (percentage of 1-h time point) ($n = 6$ biologically independent animals). Two-way ANOVA with Tukey's post

hoc test was used for comparisons among multiple groups, Control:MYnano vs. Control:SP@MYnn, $P < 0.0001$; IBS:MYnano vs. IBS:SP@MYnn, $P < 0.0001$. **h** Drug contents in the small intestinal tissues (left) and in the blood (right) at different time points among different groups ($n = 3$ biologically independent animals). Two-way ANOVA with Tukey's post hoc test was used for comparisons among multiple groups, 2:Con_MYnano vs. 2:IBS_MYnano, $P = 0.0314$; 2:Con_SP@MYnn vs. 2:IBS_SP@MYnn, $P = 0.9368$; 3:Con_MYnano vs. 3:IBS_MYnano, $P = 0.1991$; 3:Con_SP@MYnn vs. 3:IBS_SP@MYnn, $P = 0.9686$. **i** Schematic diagram of the determination of MY content. Created in BioRender. Ji, C. (<https://BioRender.com/pi8rrn4>). The data show means \pm SD (* < 0.05 , ** < 0.01 , n.s., no significance). Source data are provided as a Source Data file.

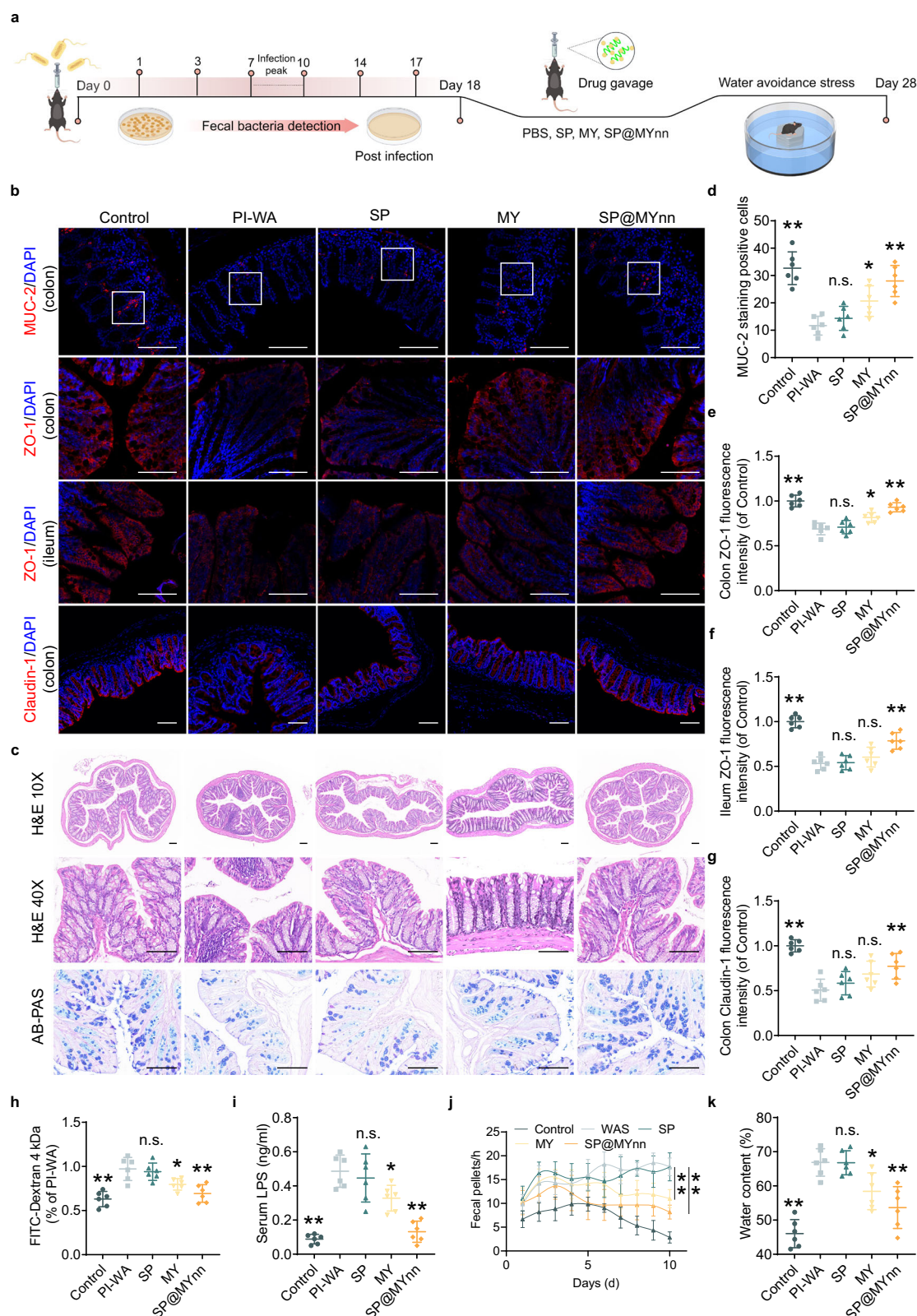
The peripheral nerve-related alterations have guided us to conduct further research on the central nervous system (Fig. 7a). In the pre-frontal cortex³⁷, the quantity of microglia cells increased significantly, which is closely associated with cognitive function. SP@MYnn achieved a more remarkable improvement effect compared with MY. After oral administration of SP@MYnn, the expression of CSF-1R and MHCII in this region was significantly downregulated compared with the PI-WA group. Subsequently, although no increase in the number of microglia was observed in the amygdala, an elevated proportion of activated microglia was identified, presenting as shortened and thickened processes and reduced coverage area. Representative images are displayed in Fig. 7c. These alterations have a close relationship with emotional processing. Simple oral administration of SP was incapable of suppressing this change, while SP@MYnn achieved a superior therapeutic effect compared with MY (Fig. 7b–g and Supplementary Fig. 24a–c). Meanwhile, the level of serum corticosterone rose and was accompanied by an increase in the adrenal index. However, there was no obvious change in the thymus index. For these phenomena, SP@MYnn brought about some improvements (Supplementary Fig. 24d–f). The sucrose preference experiment indicated that neither PI-WA nor PI-IBS mice presented obvious depressive tendencies (Supplementary Fig. 25a–b). Nevertheless, in the open field experiment, the movement distance of PI-WA mice decreased, and the duration of stay in the central area and the number of crossings also reduced, suggesting the occurrence of anxiety symptoms. The indexes of dorsal brown adipose tissue (BAT) and testicular white adipose tissue (e. WAT) in PI-WA mice both rose, which was related to chronic stress (Fig. 7h and Supplementary Fig. 25c–h). Interestingly, the number of feces of mice in the PI-WA group significantly increased in the open field test, which is highly similar to that of clinical IBS-D patients who tend to develop symptoms under stress in a new environment (Supplementary Fig. 25i). In response to these symptoms, the efficacy of MY appeared insignificant and unstable, whereas SP@MYnn restored motor ability, ameliorated anxiety and diarrhea symptoms. Furthermore, in the elevated plus maze (EPM) experiment, avoiding the interference of individual differences in motor ability, we revalidated the changes in anxiety. SP@MYnn increased the time that IBS-D mice spent exploring the open arms and the number of entries into the open arms (Fig. 7i and Supplementary Fig. 25j–k). Besides, in the hole board test, SP@MYnn significantly increased the frequency of mice exploring the holes (Supplementary Fig. 25l). Besides, the novel object recognition test (NOR) was performed to evaluate the alterations of memory and cognitive abilities. Compared with the PI-WA group, the SP@MYnn group significantly enhanced the exploration of new objects (Supplementary Fig. 25m).

SP@MYnn realizes multisystem therapy via the brain-gut axis

The colonic contents of mice in each group were taken for 16 s amplicon sequencing to analyze the composition of the gut microbiota. At the phylum level, the dysregulated ratio of *Firmicutes* and *Bacteroidetes* in the PI-WA group was mitigated after the application of SP, MY, and SP@MYnn. At the genus level, it was discovered that oral

administration of MY could enrich *Akkermansia*, and oral administration of SP simultaneously upregulated *Akkermansia* and *Lactobacillus*, both of which are recommended probiotics for IBS-D patients³⁸. And the enrichment of *Lactobacillus* was most prominent in the SP@MYnn group (Supplementary Fig. 26a–b, f–g). There was no obvious difference in microbiota diversity among the groups, but the α diversity of the PI-WA group was slightly decreased compared with the other groups. This might have clinical implications, as the pathophysiological alterations in IBS-D are inherently less intense than those in inflammatory bowel diseases (Supplementary Fig. 26c–d). SP@MYnn significantly enriched *Lactobacillus* and *Limosilactobacillus*, which might play a crucial role in regulating IBS-D symptoms. Moreover, the enriched genus such as *Blautia*³⁹ have also been indicated in studies that their metabolites may improve intestinal barrier function. The application of SP and MY also enriched several beneficial bacterial genera such as *Akkermansia*, highlighting the prebiotic potential of SP. However, in the SP@MYnn group, *Akkermansia* did not increase as it did in the MY and SP groups. This might be because SP@MYnn contains other components, such as CS, which may not have an affinity for *Akkermansia* (Supplementary Fig. 26e). The dorsal horn of the spinal cord is a crucial site for the transmission of pain signals. Afferent nerves convey pain signals from the intestinal tract to the dorsal horn of the spinal cord and then to the brain⁴⁰. The microglia in the L6-S1 dorsal horn exhibited an activated state both in terms of quantity and morphology. This phenomenon is similar to that in brain tissue and is also effectively treated by SP@MYnn (Fig. 8a–b). To clarify the mechanism by which SP@MYnn significantly improves the therapeutic effect of the CNS in IBS-D, we further conducted a metabolomics analysis of colonic contents. It was found that caproic acid, isobutyric acid, isovaleric acid, etc. were significantly elevated in the PI-WA group. Among them, isovaleric acid has even been reported as a pathogenic factor for IBS-D^{41,42} (Fig. 8c–e). The ability of butyric acid to counteract neuroinflammation and its function as an intestinal-brain interaction mediator have received numerous reports⁴³. To validate the role of butyric acid herein, we established a pseudo-sterile mouse model. When the participation of the intestinal microbiota was eliminated, the neurotherapeutic effects of SP@MYnn were significantly decreased both in terms of behavior and histology (Fig. 8f–h and Supplementary Fig. 27).

Subsequently, we conducted verification at the cellular level using IEC-6. Within the tested concentration range, SP, MY, MYnano, and SP@MYnn did not affect the viability of IEC-6. However, when the experimental concentration of sodium butyrate (NaB) exceeded 5 mM, the cell viability was significantly influenced (Supplementary Fig. 28a–e). Subsequently, the intestinal barrier was damaged by using tert-butyl hydroperoxide (TBHP), and significant upregulation of ZO-1 and Claudin-1 was observed in the MY, MYnano, SP@MYnn, and NaB groups (Supplementary Fig. 28f, h–i). Then, mouse microglial cells (BV-2) were stimulated with LPS to simulate neuroinflammation in vitro, and cell viability tests were conducted first. Since SP@MYnn and MYnano could not reach CNS in their intact forms, we instead



focused on testing the concentration-dependence of the drug effects. LPS significantly upregulated the CD86 level of BV-2, while both MY and NaB successfully reduced the activation level of microglia. To sum up, both in vivo and in vitro tests indicate that intestinal microbiota metabolites are involved in or at least partially contribute to the therapeutic effects of SP@MYnn on the intestinal and CNS (Supplementary Fig. 28g, j–l).

SP@MYnn regulates the brain-gut axis via SCFAs

To further validate whether the changes in the SCFAs metabolomics played a crucial role in the treatment, we paid attention to GPR43, a classical SCFAs receptor, and constructed *GPR43* KO mice (Fig. 9a) and *GPR43* KO BV-2 cells⁴⁴. Then, we validated that *GPR43* was successfully knocked out in the spinal cord and brain tissues (Fig. 9b). In wild-type (WT) mice, CD86 and MHCII in the spinal cord, CSF-1R and MHCII in

Fig. 5 | Intestinal barrier repair function of SP@MYnn. **a** Schematic diagram of the construction of the PI-WA model. By Figdraw. **b** MUC-2, ZO-1, Claudin-1 immunostaining. **c** Colon H&E and AB-PAS staining. **d–g** Fluorescence intensity of MUC-2 (**d**), ZO-1 (**e**, **f**), Claudin-1 (**g**). **h** Serum FITC fluorescence intensity in intestinal permeability test. **i** Serum LPS level. **j** Number of fecal pellets during the WAS period. **k** Water content of fecal matter. One-way ANOVA with Tukey's post hoc test was used for comparisons among multiple groups. For the ANOVA for MUC-2, Control vs. PI-WA, $P < 0.0001$; PI-WA vs. SP, $P = 0.8934$; PI-WA vs. MY, $P = 0.0395$; PI-WA vs. SP@MYnn, $P < 0.0001$. For the ANOVA for colon ZO-1, Control vs. PI-WA, $P < 0.0001$; PI-WA vs. SP, $P = 0.9807$; PI-WA vs. MY, $P = 0.0140$; PI-WA vs. SP@MYnn, $P < 0.0001$. For the ANOVA for colon Claudin-1,

Control vs. PI-WA, $P < 0.0001$; PI-WA vs. SP, $P = 0.9998$; PI-WA vs. MY, $P = 0.6259$; PI-WA vs. SP@MYnn, $P = 0.0003$. For the ANOVA for dextran, Control vs. PI-WA, $P < 0.0001$; PI-WA vs. SP, $P = 0.9798$; PI-WA vs. MY, $P = 0.0359$; PI-WA vs. SP@MYnn, $P = 0.0004$. For the ANOVA for LPS, Control vs. PI-WA, $P < 0.0001$; PI-WA vs. SP, $P = 0.9329$; PI-WA vs. MY, $P = 0.0347$; PI-WA vs. SP@MYnn, $P < 0.0001$. For the ANOVA for Fecal pellets, SP vs. MY, $P < 0.0001$; SP vs. SP@MYnn, $P < 0.0001$. For the ANOVA for water content, Control vs. PI-WA, $P < 0.0001$; PI-WA vs. SP, $P > 0.9999$; PI-WA vs. MY, $P = 0.0357$; PI-WA vs. SP@MYnn, $P = 0.0005$. The data show means \pm SD ($n = 6$ biologically independent animals, * < 0.05 , ** < 0.01 , n.s., no significance vs. the PI-WA group), scale bar = 100 μ m. Source data are provided as a Source Data file.

the prefrontal cortex, and CD86, CSF-1R and MHCII in the amygdala were all downregulated after the administration of SP@MYnn. Nevertheless, in *GPR43* KO mice, the downregulation of these indicators was no longer significant, but there was still a certain extent of downregulation, which might be attributed to the effect of MY per se (Fig. 9c–n). Following oral administration of SP@MYnn, the activation of microglia in WT mice was suppressed, while this therapeutic effect was no longer conspicuous in *GPR43* KO mice (Supplementary Fig. 29). A comparable phenomenon was also witnessed in the expression of CSF-1R that colocalized with microglia (Fig. 9o). Subsequently, when SP@MYnn and NaB were administered to LPS-stimulated BV-2 cells, *GPR43* KO BV-2 cells were no longer susceptible to NaB treatment, while SP@MYnn still exerted a certain effect, which was in line with the previous cellular experiments (Fig. 9p and Supplementary Fig. 30).

Discussion

Our engineered microalgae drug delivery biosystem (SP@MYnn) was devised to overcome the current limitations of oral drug delivery systems in the treatment of IBS-D. The bioinformatics analysis and experimental validation of the existing dataset highlighted the deficiencies of conventional drugs and encapsulation approaches (such as free drugs and traditional capsule preparations) in coping with the pharmacokinetic challenges presented by IBS-D⁴⁵. IBS-D exhibits alterations in intestinal motility, typically characterized by intensified peristalsis, disordered contractions⁴⁶, and severely undermines the bioavailability of drugs that rely on food interactions and initial metabolism in the small intestine for absorption. Common drug delivery systems⁴⁷, including liposomes, polymeric nanoparticles, and hydrogels, have been employed in various circumstances but have demonstrated significant limitations in IBS-D, such as limited ability to target specific intestinal regions, particularly in cases of altered transit times. A clinical trial concerning intestinal gel has been conducted and diarrhea symptoms are controlled through the adsorption of intestinal toxins by porous hydrogel. However, it is not advised to be used in combination with drugs since it may impede the release of the drugs⁴⁷. Our biosystem exploits the distinctive helical structure of microalgae and further boosts tissue adhesion through micro-nano modifications, achieving an efficient engineered microbial-nano biosystem targeting IBS-D and facilitating drug delivery.

Our research adopted a model that combined CR infection with WAS, which simulated the multifactorial etiology of IBS-D more precisely than single-factor models. This model effectively replicated the clinical manifestations of IBS-D, encompassing intestinal barrier dysfunction, mast cell activation, and neuropsychiatric symptoms, without significant inflammatory pathology⁴⁸. Our study demonstrated that SP@MYnn showed therapeutic efficacy in both the CR infection alone and the CR infection combined with WAS models, suggesting that SP@MYnn has extensive clinical applicability for IBS-D with diverse etiologies. Furthermore, when establishing a PI-IBS animal model, different studies might employ *Shigella spp.*, *Salmonella spp.*, *Campylobacter spp.*, etc. In contrast, CR is a pathogen specific to mice, and its infection can generate pathophysiological changes similar to human intestinal infections, particularly intestinal barrier functional impairment and mild inflammatory

responses⁴⁹. Moreover, after CR infection, it is less likely to progress to severe systemic inflammation, making it suitable for simulating the mild inflammatory state in PI-IBS and having higher safety, which is more in line with the clinical characteristics of PI-IBS⁵⁰. Currently, the clinical treatment of IBS-D, encompassing anti-spasmodic, antidiarrheal, and receptor antagonists, primarily offers symptomatic relief, with limited long-term efficacy and fails to address the multi-faceted nature of IBS-D involving both gastrointestinal and neurological symptoms²⁰. For instance, rifaximin, a recommended therapeutic modality, is limited by its short-term efficacy and restricted application in broader symptom management⁵¹. IBS-D, as one of the diseases with the most pronounced and closely related intestinal-brain temporal and spatial symptoms, is an extremely appropriate option for treatment when contemplated from the perspective of the brain-gut axis⁷. SP@MYnn not only effectively delivers MY to the intestinal tract but also leverages the prebiotic properties of SP to enhance the composition of the intestinal microbiota and the generation of beneficial SCFAs such as butyric acid⁵², addressing both intestinal and neurological symptoms via the gut-brain axis and offering a more comprehensive approach to the treatment of IBS-D. Additionally, isovaleric acid has been demonstrated to partially mediate visceral hypersensitivity responses⁴¹. And notably, the content of isovaleric acid was also notably increased in our model. SP@MYnn significantly reduced the content of isovaleric acid, which not only attests to the effectiveness of the biosystem but also indicates the alignment of our animal model with the key points of clinical research.

Each constituent of SP@MYnn plays a vital role in surmounting the inherent challenges in the treatment of IBS-D. Numerous studies have emphasized the role of mast cells in IBS-D and described the disease from the perspectives of allergy and immune disruption²¹. MY is renowned for its anti-inflammatory and immunomodulatory effects¹⁷. However, its bioavailability in the gastrointestinal tract is low and unstable and encapsulation with PLGA enhances its stability and dispersion⁵³. SP offers bioadhesive properties, supports targeted binding to villi, and provides prebiotic activity for regulating the intestinal microbiota²⁵. The positively charged CS coating further stabilizes the entire biosystem in the acidic gastric environment, enhances adhesion to intestinal tissues, and possesses antibacterial properties³³, which is beneficial for IBS-D patients with SIBO. Admittedly, the condition of SIBO is highly complex, and SP@MYnn might not be applicable to all circumstances⁵⁴. These synergetic effects support a robust multi-target approach and address the distinctive pharmacokinetic and therapeutic challenges of IBS-D.

In conclusion, our research emphasizes the potential of SP@MYnn as a safe and effective therapeutic strategy for IBS-D. Each component of SP@MYnn exhibits a high degree of biological safety. PLGA, CS, and SP have been approved for oral use by the FDA and other global regulatory agencies, supporting its translational potential^{53,55,56}. Admittedly, there is still scope for in-depth exploration in our research. Currently, a comprehensive large animal model that accurately reflects the disease characteristics of clinical IBS-D patients has not been identified. Researches was confined to clinical samples and small animal studies, which has constrained the advancement of IBS-D research.

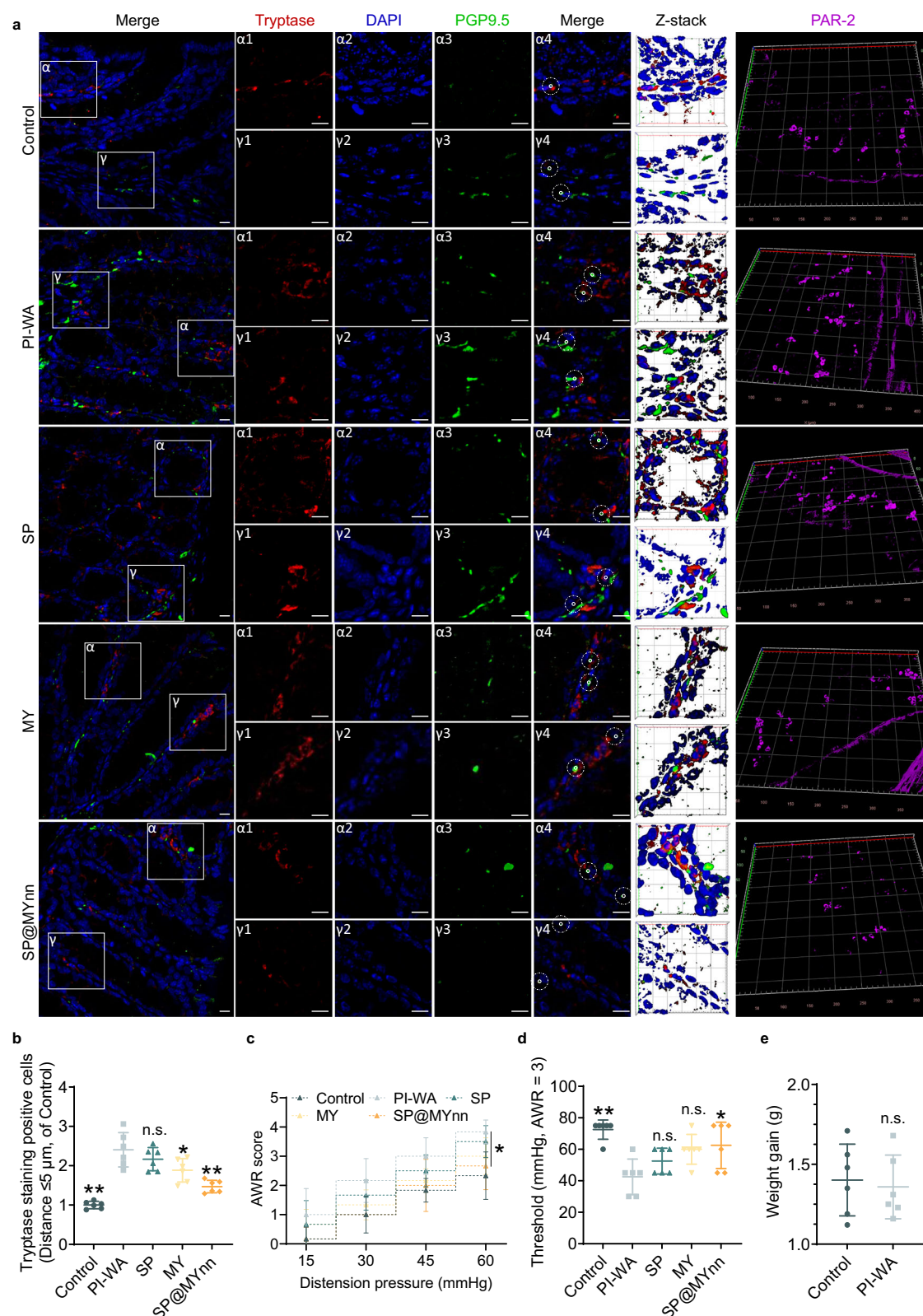
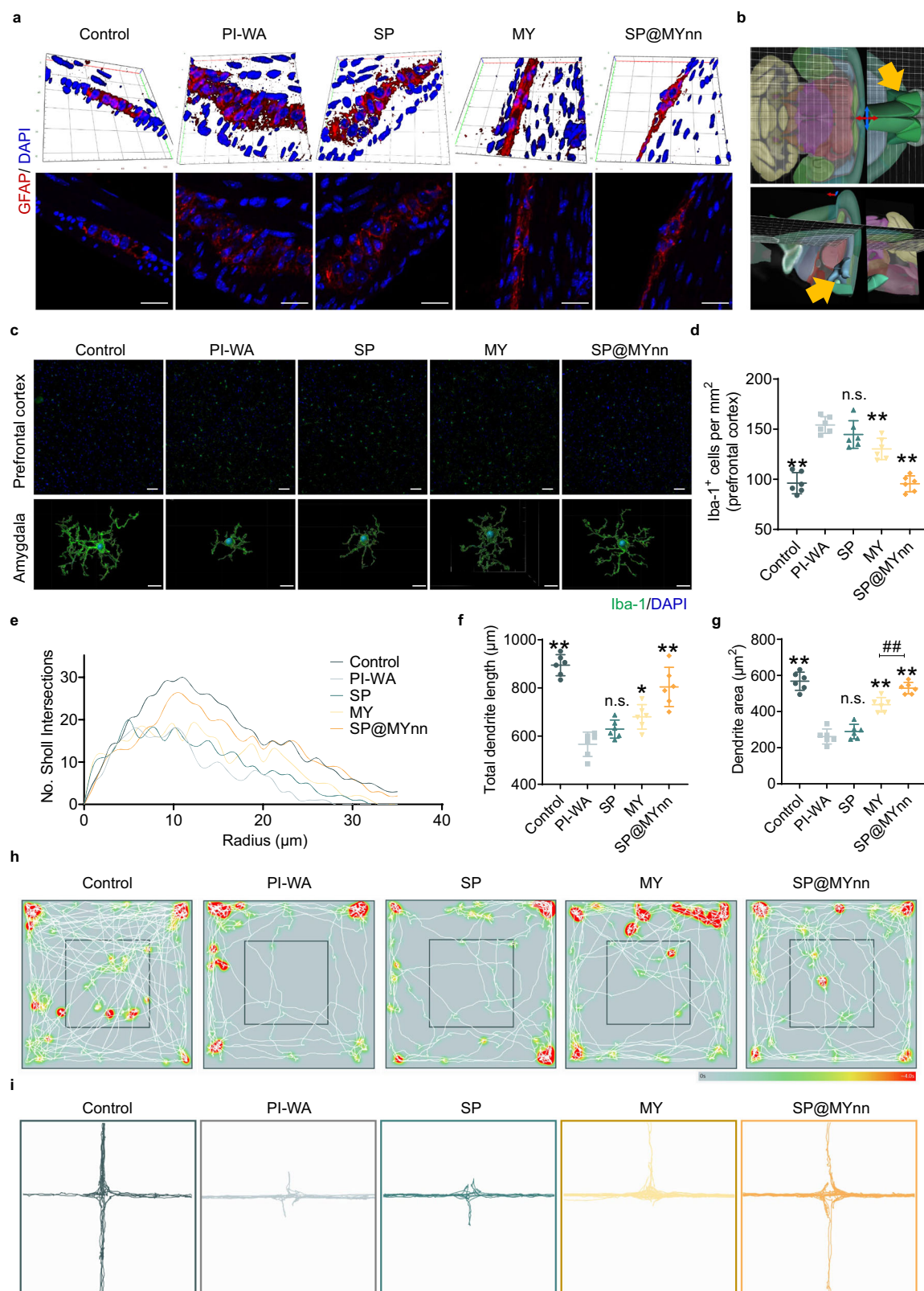


Fig. 6 | SP@MYnn suppresses visceral hypersensitivity caused by mast cell activation. **a** Colon Tryptase (red), PGP9.5 (green), Par-2 (purple), and DAPI (blue) immunostaining. **b** Counting of Tryptase-positive cells at a distance less than 5 μ m from the neural tissue. **c** The AWR score under different colorectal pressures. **d** The colorectal pressure reaching the pain threshold. One-way ANOVA with Tukey's post hoc test was used for comparisons among multiple groups. For the ANOVA for tryptase, Control vs. PI-WA, $P < 0.0001$; PI-WA vs. SP, $P = 0.5984$; PI-WA vs. MY, $P = 0.0286$; PI-WA vs. SP@MYnn, $P < 0.0001$. For the ANOVA for tryptase,

PI-WA vs. SP@MYnn, $P = 0.0393$. For the ANOVA for threshold, Control vs. PI-WA, $P = 0.0003$; PI-WA vs. SP, $P = 0.4714$; PI-WA vs. MY, $P = 0.0522$; PI-WA vs. SP@MYnn, $P = 0.0205$. **e** The weight gain value during the WAS period. Two-tailed unpaired t-tests were used for comparisons between two groups, $P = 0.7316$. The data show means \pm SD ($n = 6$ biologically independent animals, * < 0.05 , ** < 0.01 , n.s., no significance vs. the PI-WA group), scale bar = 10 μ m. Source data are provided as a Source Data file.



Methods

1. Ethical statement

All animal studies were approved by the Institutional Animal Care and Use Committee of Zhejiang University (AIRB-2021-952) and were carried out in accordance with the National Institutes of Health Guide for the Care and Use of Laboratory Animals.

Reagents and antibodies

The relevant details can be found in Supplementary Table 1.

Bioinformatics analysis

The chip data with the identifier GSE36701 was retrieved from the NCBI GEO database, and its chip platform was GPL570. In this chip, there

Fig. 7 | The regulatory role of SP@MYnn on psychiatric symptoms. **a** GFAP immunostaining and 3D images, scale bar = 10 μ m. **b** Position of prefrontal cortex and amygdaloid. **c** Iba-1 immunostaining of prefrontal cortex (scale bar = 50 μ m) and 3D reconstruction of microglia in amygdaloid (scale bar = 10 μ m). **d** Density of Iba-1 positive cells in prefrontal cortex. **e–g** Sholl analysis (e), dendrite length (f) and dendrite area (g) of microglia in this region. One-way ANOVA with Tukey's post hoc test was used for comparisons among multiple groups. For the ANOVA for Iba-1 positive cells, Control vs. PI-WA, $P < 0.0001$; PI-WA vs. SP, $P = 0.5257$; PI-WA vs. MY, $P = 0.0046$; PI-WA vs. SP@MYnn, $P < 0.0001$; MY vs. SP@MYnn, $P < 0.0001$. For

the ANOVA for dendrite length, Control vs. PI-WA, $P < 0.0001$; PI-WA vs. SP, $P = 0.3013$; PI-WA vs. MY, $P = 0.0112$; PI-WA vs. SP@MYnn, $P < 0.0001$. For the ANOVA for dendrite area, Control vs. PI-WA, $P < 0.0001$; PI-WA vs. SP, $P = 0.7686$; PI-WA vs. MY, $P < 0.0001$; PI-WA vs. SP@MYnn, $P < 0.0001$; MY vs. SP@MYnn, $P = 0.0059$. **h, i** The merge map of the open field experiment (h) and the trajectory map of EPM (i). The data show means + SD ($n = 6$ biologically independent animals, * < 0.05 , ** < 0.01 , n.s., no significance vs. the PI-WA group, ## < 0.01). Source data are provided as a Source Data file.

were 15 cases of PIBS samples (post infection IBS, unknown time point and organism), 28 cases of PIBD samples (post *Campylobacter* infection with IBS, within 6 months), and 53 cases of IBS-D samples (IBS dominated by diarrhea). These samples were respectively compared with the HV (healthy volunteer) samples of the same batch to screen for differential genes ($FC \geq 1.2$ and P value < 0.05). Subsequently, GO and KEGG functional enrichments were conducted.

The pharmacokinetics of MY@Cap and FITC@Cap

The enteric capsule equipment and raw materials were purchased from Yuyan Medical Instrument Company (Shanghai, China), and detailed usage strategies can be found on the brand's official website: (<http://www.yuyanbio.com>). Free drugs and capsule formulations were respectively administered orally to the IBS-D model (the modeling approach is described in "Construction of IBS-D model") and the control model. Among them, MY@Cap was used to study the blood drug concentration, and FITC@Cap was used to study the in vivo distribution.

Grouping Information: 1. Con_MY: Normal mice were given gavage to free MY; 2. Con_MY@Cap: Normal mice were given gavage to Capsule form of MY; 3. IBS_MY: IBS-D mice were given gavage to free MY; 4. IBS_MY@Cap: IBS-D mice were given gavage to Capsule form of MY.

Synthesis of SP@MYnn

The synthesis process can be classified into three steps. First step: Synthesis of MY@PLGA. Dissolve MY (5 mg) and PLGA (50 mg) in dichloromethane (DCM, 1 ml), prepare 2% polyvinyl alcohol (PVA, 2 ml) using deionized water and add it to the upper layer of DCM. After emulsification with a probe ultrasonic device (200 W, 10 min), the solution was stirred at room temperature for 8 h to volatilize DCM. Collect MY@PLGA (18840 g, 10 min) by centrifugation and rinse with deionized water to remove unreacted reagents.

Second step: Synthesis of MYnano. CS (substitution degree 98%, 50 mg) was dissolved in deionized water (5 ml) and added to the MY@PLGA solution. The mixture was stirred at room temperature for 4 h. Subsequently, the centrifugation and washing procedures as mentioned above were adopted to collect MYnano.

Third step: Synthesis of SP@MYnn. SP (25 mg) was cleaned with phosphate buffered saline (PBS), then added to the resuspended MYnano solution and the reaction was stirred for 60 min. Finally, SP@MYnn was collected through centrifugation (2780 g, 5 min) and washing.

For the preparation of DiO-labeled materials, it is only necessary to dissolve DiO (1 mg) in Dimethyl sulfoxide (DMSO, 0.1 ml) and then add it to the DCM mixture in the first step.

Characterization of MY@PLGA, MYnano, SP@MYnn

For MYnano and MY@PLGA, the hydrodynamic diameters and surface charges were measured by the dynamic light scattering system (Malvern Panalytical Zetasizer Nano ZS90, UK), and the spectra were acquired using the UV-visible-near infrared spectrometer (Shimadzu UV-2600, Japan). After negative staining with phosphotungstic acid, the morphology was observed via TEM (FEI Tecnai F20, USA). For SP and SP@MYnn, the surface charges were measured by the same equipment mentioned above. The morphological characteristics were observed using SEM (Hitachi SU-70, Japan) and upright fluorescence

microscope (Nikon, Japan), and 3D scanning was performed and the thickness of the nano-coating was calculated using laser confocal microscope (Zeiss LSM880, Germany). The procedure for determining EE%: MYnano suspension was homogeneously mixed with the mixed solution containing NaOH (0.1 M) and SDS (0.5%) at a volume ratio of 1:10, and was oscillated in a 70 °C water bath for 30 minutes to thoroughly hydrolyze the PLGA framework and release the encapsulated MY. Subsequently, the mixture was centrifuged at 16040 g for 15 minutes to remove PLGA degradation debris. The supernatant was taken as the sample to be tested, and the percentage of MY content in the total dosage was calculated based on the standard curve. For the measurement of EE% of SP@MYnn, we initially centrifuged at 1000 g for 5 minutes to remove SP@MYnn, and then determined the unbound MYnano in the supernatant to calculate the final EE%. DiO-labeled MY@PLGA and MYnano were co-incubated with IEC-6 cells, and the fluorescence intensity of the IEC-6 cell membrane at different time points was recorded to assess the cell uptake efficiency.

In vitro simulation of drug release

At 37 °C, MYnano and SP@MYnn were successively placed in adequate amounts of SGF, SIF and SCF, and retrieved at the requisite time points. They were respectively utilized for optical microscopy or SEM observation, calculation of the drug release amount, and determination of the nano-coating thickness by LSM880.

In vivo distribution and drug release

In this part, experiments were mainly conducted using DiO-labeled materials. Eight-week-old BALB/c Nude mice were selected for gavage administration. At the required different time points, fluorescence images of the living and ex vivo samples were collected using PhotonIMAGER™ (Biospace, USA). Intestinal tissues at specific time points are subjected to frozen section observation, and intestinal contents are used for SEM observation.

In vitro adhesion simulation of intestinal mucus layer

Mucin was spin-coated (at 3000 rpm for 20 s) on the surface of Au crystals to simulate the intestinal mucus layer. Equal amounts of MY@PLGA and MYnano were introduced into the chamber at the same rate using a QCM (Biolin QSense® Explorer, Sweden) to measure ΔF .

Everted sac of small intestinal

Equal-length sections of the same part of the small intestine were prepared and inverted to expose the villi outward. They were fully covered with the same amount of DiO-labeled material. Subsequently, they were placed in a shaker incubator at 37 °C for shaking and incubation to simulate the scouring of intestinal fluid. Finally, fluorescence images were captured using a PhotonIMAGER™.

Preparation of biological samples for SEM

The samples were fixed in 2.5% glutaraldehyde solution at 4 °C overnight and then washed three times with PBS for 15 min each. Subsequently, the samples were fixed in 1% osmium acid for 1–2 h and washed with PBS three times. Then, the samples were dehydrated with ethanol of different concentrations and subsequently dehydrated using critical point dryer (Hitachi HCP-2, Japan). Before observation,

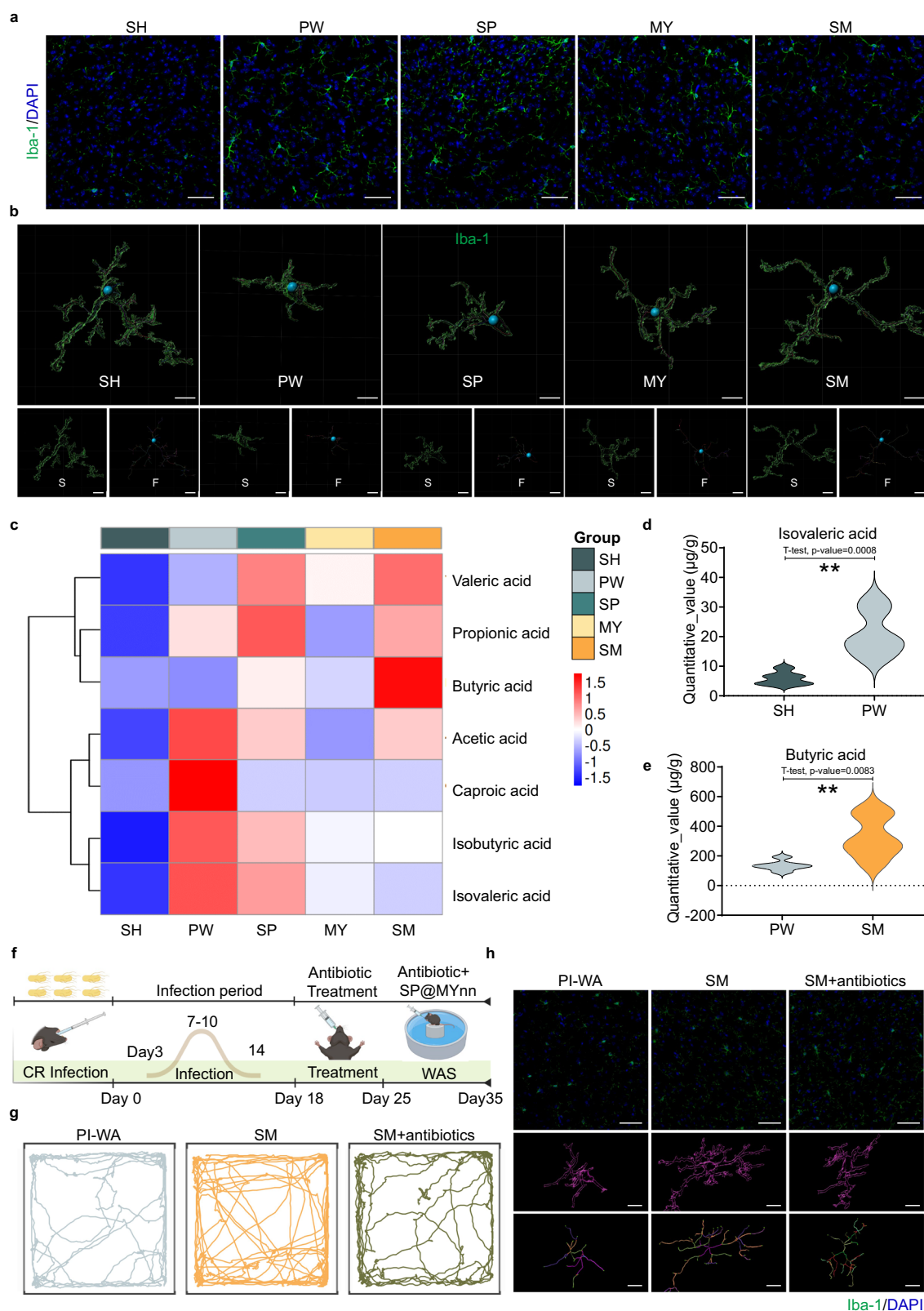


Fig. 8 | The effect of the brain-gut axis of SP@MYnn. a–b Iba-1 immunostaining (a, scale bar = 50 μ m) and 3D reconstruction (b, scale bar = 10 μ m) of dorsal horn of spinal cord. **c** Heatmap of SCFAs in colonic contents. **d** Comparison of isovaleric acid content between control group and PI-WA group. **e** Comparison of butyric acid content between SP@MYnn group and PI-WA group. **f–g** Schematic diagram of antibiotic experiment (f) and Open field test (g). Created in BioRender. Ji, C. (2025)

<https://BioRender.com/dravv49>. **h** Prefrontal cortex Iba-1 immunostaining, scale bar = 50 μ m, and amygdaloid nucleus Iba-1 immunostaining 3D reconstruction, scale bar = 10 μ m. Two-tailed unpaired t-tests were used for comparisons between two groups. SH, Control; PW, PI-WA; SM, SP@MYnn. n = 6 biologically independent animals, * < 0.05, ** < 0.01, n.s., no significance vs. the PI-WA group, ### < 0.01. Source data are provided as a Source Data file.

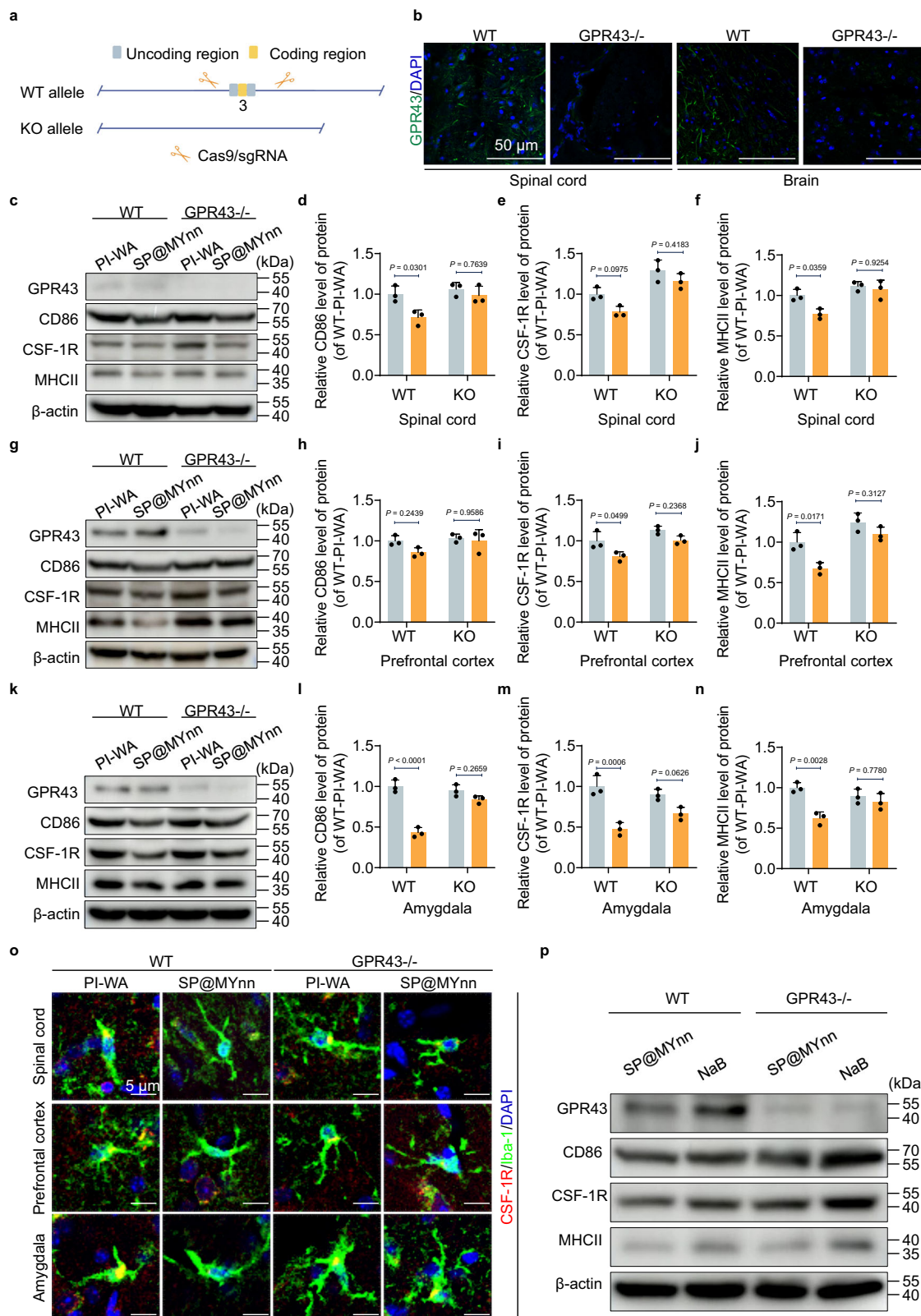


Fig. 9 | SP@MYnn regulates the brain-gut axis through SCFAs. **a** Schematic illustration of the construction of *GPR43* KO mice. **b** Immunofluorescence of GPR43 in the spinal cord and brain tissue of WT mice and KO mice, scale bar = 50 μ m. **c-n** Western blotting and quantitative analysis showing the expression of GPR43, CD86, CSF-1R and MHCII in spinal cord (c-f), prefrontal cortex (g-j) and amygdala (k-n). Two-way ANOVA with Tukey's post hoc test was used for comparisons

among multiple groups. **o** CSF-1R and Iba-1 immunofluorescence staining of spinal cord, prefrontal cortex and amygdala, scale bar = 5 μ m. **p** Western blotting showing the expression of GPR43, CD86, CSF-1R and MHCII in WT and *GPR43* KO mice treated with SP@MYnn or NaB. The data show means + SD ($n = 3$ biologically independent animals or cells). Source data are provided as a Source Data file.

the samples were subjected to ion sputtering with an ion sputtering coater (Hitachi E-1010, Japan) for 5 min.

Infection experiment of *Salmonella typhimurium*

Salmonella typhimurium was employed to test the therapeutic potential of the materials for SIBO. Briefly, streptomycin (1 g/kg) was administered intragastrically to mice 24 h in advance to provide the ecological niche necessary for colonization. Different therapeutic interventions were administered once daily on the second day and continued for 4 days. Intestinal tissues were collected for immunofluorescence staining.

Grouping Information: 1. *Salmonella* + PBS; 2. *Salmonella* + SP (250 mg/kg); 3. *Salmonella* + MY (50 mg/kg); 4. *Salmonella* + SP@MYnn (50 mg MY/kg).

Ink propulsion experiment

After intragastric administration of 200 μ L of India ink to IBS-D mice for 15 min and 30 min, the entire small intestine and colon from the distal pylorus to the anus were isolated to observe the distance of ink propulsion. The “Ink part of whole small intestine” refers to the percentage of the farthest distance that ink has advanced in relation to the total length of the small intestine.

In-vivo distribution and pharmacokinetics in the IBS-D model

DiO-labeled MYnano and SP@MYnn were intragastrically administered to IBS-D mice. Likewise, PhotonIMAGER™ was employed to acquire fluorescence images of both in vivo and ex vivo. Intestinal tissues from different sites were observed under fluorescence microscope and SEM. Blood samples and intestinal tissues were taken to measure the drug concentrations, with the specific methods detailed in “Determination of MY content”.

Determination of MY content

The detailed usage of the instrument has been reported previously²⁶. Briefly, mice were fasted for 12 h and then intragastrically administered MYnano and SP@MYnn. Tissues and blood were collected at various time points after administration, and were respectively made into homogenates and serum followed by centrifugation (4500 g, 10 min). To 50 μ L of intestinal homogenates or serum, 150 μ L of acetonitrile was added to precipitate proteins. After thorough mixing, centrifugation (4500 g, 10 min) was performed again. The resulting supernatant was immediately collected and detected using an Agilent 1290 series (Agilent, Waldbronn, Germany).

Grouping Information: 1. Con_MYnano: Normal mice were given gavage to MYnano; 2. Con_SP@MYnn: Normal mice were given gavage to SP@MYnn; 3. IBS_MY: IBS-D mice were given gavage to MYnano; 4. IBS_SP@MYnn: IBS-D mice were given gavage to SP@MYnn.

Animal experiments

Except for the live imaging, which employed 8-week-old BALB/c Nude female mice, all the remaining experiments utilized 5-week-old C57BL/6J male mice. The mice were reared under SPF conditions and purchased from Beijing Vital River Laboratory Animal Technology Co., Ltd. GPR43-KO mice (Strain NO. T003292) were purchased from GemPharmatech (Nanjing, China). The animal feed was purchased from Jiangsu Xietong Co., Ltd. (<https://www.jsxtsw.com/>). Feed with item number 1010019 was used for immunodeficient mice, and feed with item number XT101ZJ-012 was used for other experimental mice. All animals were housed under specific pathogen-free (SPF) conditions. The light/dark cycle was set to 12 h each. The animals were housed at a temperature of 20–26 °C and a relative humidity of 40%–70%.

Construction of IBS-D model

Overall, it is divided into two parts, namely CR infection and the subsequent WAS procedure. CR infection: CR was expanded by

culturing in Luria Broth medium at 37 °C, and each mouse was orally administered with 2×10^9 CFU. Fecal samples were collected after infection and plated on Macconkey agar plates to evaluate the infection status.

WAS procedure: After the infection completely disappeared, the mice were placed on an elevated platform 1 cm above the water surface for 10 consecutive days, for 1 h each day. To minimize diurnal variations, WAS was only performed between 9 am and 11 am. The control group was also placed on the platform, with no water around it (sham WAS). Treatment (PBS, SP, MY, SP@MYnn) was carried out after the daily WAS. The number of defecations of mice in the WAS was recorded, and the moisture content of feces was measured after the experiment was completed.

Grouping information for verifying the efficacy of SP@MYnn

1. Control: Normal mice were given gavage to PBS;
2. PI-WA: The treatment administered to IBS-D mice was an equal volume of PBS as that of the drug group;
3. SP: The treatment administered to IBS-D mice was SP (250 mg/kg);
4. MY: The treatment administered to IBS-D mice was MY (50 mg/kg).
5. SP@MYnn: The treatment administered to IBS-D mice was SP@MYnn (50 mg MY/kg).

The operation procedures of various kits

Detailed experimental process descriptions for various kits are available on the official products. The brands and item numbers are listed in Supplementary Table 1.

Intestinal permeability in vivo

The paracellular permeability of intestinal cells was assessed using Four kDa FITC-Dextran. Briefly, mice were gavaged with sterile 1X PBS containing FITC-Dextran (0.2 ml, 75 mg/ml). Serum samples were collected 5 h later and fluorescence was detected using the SpectraMax® iD5 (Molecular Devices, USA) (Excitation wavelength: 485 nm; Emission wavelength: 522 nm).

AWR

After brief isoflurane anesthesia, a pediatric disposable silicone balloon catheter was inserted into the rectum, with the balloon positioned 2.5 – 3 cm from the anal verge and fixed in place. Thirty min after the mice recovered and adapted, colorectal dilation was gradually performed. Four pressures (15, 30, 45, and 60 mmHg) were applied in sequence, each lasting for 20 seconds with an interval of 5 min. The pain threshold was defined as AWR = 3, and detailed information on the AWR scoring is provided in Supplementary Table 2.

Western blot

Proteins were isolated from tissue homogenates and cultured cells. Briefly, proteins were transferred onto polyvinylidene difluoride (PVDF) membranes. Subsequently, the membranes were blocked with 5% non-fat milk for 2 h and then incubated overnight at with each primary antibody. After being washed three times with Tris-buffered saline with Tween 20 (TBST), the membranes were incubated with the horseradish peroxidase (HRP)-conjugated secondary antibody for 1 h at room temperature. Signals were detected using the ChemiDoc XRS+ imaging system (Bio-Rad). Band densities were measured and quantified using ImageJ software. The full-membrane images of all the Western blotting experiments presented in this paper can be inspected in Source Data.

Immunofluorescence and immunohistochemistry

Mouse tissues were collected in accordance with the approved ethical guidelines. Mice were anesthetized with isoflurane, and PBS

and 4% paraformaldehyde (PFA) were perfused through the heart. The tissues were fixed in 4% PFA for 24 h at 4 °C. Both paraffin embedding and cryoembedding were carried out in accordance with standard procedures. For fluorescence staining, after blocking with 5% bovine serum albumin (BSA) for 30 min, the sections were incubated with the primary antibody at 4 °C overnight. After washing, the corresponding fluorescent secondary antibody was used to incubate the sections at room temperature for 2 h, and the cell nuclei were stained with DAPI.

For cell experiment, after fixation, cells were permeabilized with 0.1% Triton X-100 for 5 min. The remaining steps were the same as described above.

For paraffin sections, sodium citrate buffer or EDTA buffer was selected for antigen retrieval based on the characteristics of the antibody. Immunohistochemistry employed DAB chromogenic reaction and hematoxylin staining.

Microglial sholl analysis

Sholl analysis was conducted using Imaris (Batch) 9.7 with the Sholl Analysis plugin. Concentric circles were drawn at intervals of 1 µm from the cell body, and the intersections with microglial processes were quantified. The analyzed data were used to assess the branch complexity and dendritic patterns.

Behavioral experiment

The relevant details can be found in Supplementary Table 3.

Targeted metabolomics

GC analysis was conducted using a Trace 1300 gas chromatograph (Thermo Fisher Scientific, USA). Mass spectrometry detection of metabolites was carried out on an ISQ 7000 (Thermo Fisher Scientific, USA). GC analysis conditions: GC analysis was performed on a Trace 1300 gas chromatograph (Thermo Fisher Scientific, USA). The gas chromatographic column was an Agilent HP-INNOWAX capillary column (30 m × 0.25 mm ID × 0.25 µm), with helium as the carrier gas at a flow rate of 1 mL/min. The injection ratio was 10:1, the injection volume was 1 µL, and the injection temperature was 250 °C. The ion source temperature was 300 °C, and the mass spectrometry transfer line temperature was 250 °C. The column temperature was programmed to increase from the initial temperature of 90 °C, then rise at a rate of 10 °C/min to 120 °C, increase at a rate of 5 °C/min to 150 °C, and finally increase at a rate of 25 °C/min to 250 °C and hold for 2 min. Mass spectrometry conditions: Mass spectrometry detection of metabolites was performed on an ISQ 7000 (Thermo Fisher Scientific, USA) using the electron impact ionization mode. The single ion monitoring (SIM) mode was employed, with an electron energy of 70 eV.

Antibiotic treatment

On the basis of the construction of the IBS-D model, antibiotics (ampicillin at 0.3 mg/ml, streptomycin at 2.5 mg/ml, and colistin at 0.3 mg/ml) were used continuously for a total of 17 days after the eradication of the CR infection.

Cell experiments

BV-2 cells (Cat# iCell-m011, Cellverse Bioscience Technology) were cultivated in high glucose DMEM medium, and IEC-6 cells (Cat# iCell-r016, Cellverse Bioscience Technology) were grown in the medium supplemented with 0.01 mg/ml bovine insulin. All the media were supplemented with 10% fetal bovine serum and 1% penicillin-streptomycin. Except for the concentration-dependent experiments, the detailed information of different intervention methods is as follows. 1. Control: basal medium; 2. TBHP (200 µM); 3. SP (79.5 µg/mL); 4. MY (15.9 µg/mL); 5. MYnano (15.9 µg MY/mL); 6. SP@MYnn (15.9 µg MY/mL); 7. NaB (2 mM); 8. LPS (1 µg/mL).

DNA Extraction and 16S rRNA Gene Amplicon Sequencing

OMEGA Soil DNA Kit (Omega Bio-Tek, USA) was used to extract total genomic DNA. Subsequently, NanoDrop NC2000 spectrophotometer (Thermo Fisher Scientific, USA) and agarose gel electrophoresis were used to evaluate its quality. The V3-V4 region of the bacterial 16S rRNA gene was amplified using the forward primer 338 F (5'-ACTCC-TACGGGAGGCAGCA-3') and the reverse primer 806 R (5'-GGAC-TACHVGGGTWTCTAAT-3'). Vazyme VAHTSTM DNA Clean Beads (Vazyme, China) were used to purify the amplified products. And Quant-iT PicoGreen dsDNA Assay Kit (Invitrogen, USA) was employed for quantitative analysis. After that, amplified products were pooled equally, and pair-end 2 × 250 bp sequencing was performed using the Illumina NovaSeq platform with NovaSeq 6000 SP Reagent Kit (500 cycles).

Sequence analysis

Microbiome bioinformatics were performed with QIIME2 2019.4. Briefly, the demux plugin and the cutadapt plugin were respectively used for demultiplexing of the original sequence data and primer cutting. Next, the DADA2 plugin was used to perform quality filtering, noise removal, merging, and chimera removal on the sequences. Non-single amplification sequence variants (ASVs) were aligned using mafft and then taxonomy was assigned to ASVs using feature-classifier plugin against the SILVA Release 132 Database. Subsequently, ASV-level alpha diversity indices, such as Shannon diversity index and Simpson index were calculated using the ASV table in QIIME2, and it was plotted as a box plot. Using abundance curves to compare the richness and evenness of ASVs among groups.

Statistics and reproducibility

Two groups of data were compared using a two-sided Student's t-test. One-way anova and Tukey's post hoc analysis were employed to compare data from more than two groups. For the analysis of microbiota alpha diversity and LefSe, the Wilcoxon test was employed to compare the differences between the two groups, and the Kruskal-Wallis test was utilized to compare the differences among multiple groups. Statistical tests were processed using GraphPad Prism v.9.0 unless otherwise specified, and exact *P* values are provided in the figures whenever available (when *P* values are smaller than 0.0001, *P* < 0.0001 is shown, as the exact *P* value is not available in GraphPad Prism). The experiments in Figs. 1g; and 2a, e, k; 3a; 4c; 9b, o, p were independently repeated three times and the experiments in Fig. 2h, j; 5b, c; 7a was independently repeated six times with similar results.

Reporting summary

Further information on research design is available in the Nature Portfolio Reporting Summary linked to this article.

Data availability

The microarray data used in this study are available in the GEO database under accession code [GSE36701](#). The 16 s amplicon sequencing data generated in this study have been deposited in the SRA database under accession code [PRJNA1268130](#). The mass spectrometry data generated in this study have been deposited in the MetaboLights database under accession code [MTBLS12537](#). Source data are provided with this paper.

References

1. Chey, W. D., Kurlander, J. & Eswaran, S. Irritable bowel syndrome: a clinical review. *JAMA* **313**, 949–958 (2015).
2. Black, C. J. & Ford, A. C. Global burden of irritable bowel syndrome: trends, predictions and risk factors. *Nat. Rev. Gastroenterol. Hepatol.* **17**, 473–486 (2020).
3. Whitehead, W. E. et al. Comorbidity in Irritable Bowel Syndrome. *Am. J. Gastroenterol.* **102**, 2767–2776 (2007).

4. Ford, A. C., Sperber, A. D., Corsetti, M. & Camilleri, M. Functional gastrointestinal disorders 2 irritable bowel syndrome. *LANCET* **396**, 1675–1688 (2020).
5. Vanuytsel, T., Bercik, P. & Boeckxstaens, G. Understanding neuroimmune interactions in disorders of gut-brain interaction: from functional to immune-mediated disorders. *GUT* **72**, 787–798 (2023).
6. Gracie, D. J., Hamlin, P. J. & Ford, A. C. The influence of the brain-gut axis in inflammatory bowel disease and possible implications for treatment. *Lancet Gastroenterol. Hepatol.* **4**, 632–642 (2019).
7. Margolis, K. G., Cryan, J. F. & Mayer, E. A. The microbiota-gut-brain axis: from motility to mood. *Gastroenterology* **160**, 1486–1501 (2021).
8. Zheng, L. et al. Pinaverium reduces symptoms of irritable bowel syndrome in a multicenter, randomized, controlled trial. *Clin. Gastroenterol. Hepatol.* **13**, 1285–1292.e1281 (2015).
9. Razavi, S., Janfaza, S., Tasnim, N., Gibson, D. L. & Hoorfar, M. Microencapsulating polymers for probiotics delivery systems: Preparation, characterization, and applications. *Food Hydrocoll.* **120**, 106882 (2021).
10. Vasant, D. H. et al. British society of gastroenterology guidelines on the management of irritable bowel syndrome. *GUT* **70**, 1214–1240 (2021).
11. Dionne, J. et al. A Systematic review and meta-analysis evaluating the efficacy of a gluten-free diet and a low FODMAPs diet in treating symptoms of irritable bowel syndrome. *Am. J. Gastroenterol.* **113**, 1290–1300 (2018).
12. Camilleri, M. Diagnosis and treatment of irritable bowel syndrome a review. *JAMA* **325**, 865–877 (2021).
13. Yuan, Y., Wang, X., Huang, S., Wang, H. & Shen, G. Low-level inflammation, immunity, and brain-gut axis in IBS: unraveling the complex relationships. *Gut Microbes* **15**, 2263209 (2023).
14. Vivinus-Nébot, M. et al. Functional bowel symptoms in quiescent inflammatory bowel diseases: role of epithelial barrier disruption and low-grade inflammation. *GUT* **63**, 744–752 (2014).
15. Stillhart, C. et al. Impact of gastrointestinal physiology on drug absorption in special populations—an UNGAP review. *Eur. J. Pharm. Sci.* **147**, 105280 (2020).
16. Cash, B. D., Epstein, M. S. & Shah, S. M. A novel delivery system of peppermint oil is an effective therapy for irritable bowel syndrome symptoms. *Dig. Dis. Sci.* **61**, 560–571 (2016).
17. Song, X. M. T. et al. Myricetin: a review of the most recent research. *Biomed. Pharmacother.* **134**, 111017 (2021).
18. Park, H. H. et al. Flavonoids inhibit histamine release and expression of proinflammatory cytokines in mast cells. *Arch. Pharm. Res.* **31**, 1303–1311 (2008).
19. Rakha, A. et al. Anti-inflammatory and anti-allergic potential of dietary flavonoids: A review. *Biomed. Pharmacother.* **156**, 113945 (2022).
20. Enck, P. et al. Irritable bowel syndrome. *Nat. Rev. Dis. Prim.* **2**, 16014 (2016).
21. Gao, J., Xiong, T., Grabauskas, G. & Owyang, C. Mucosal serotonin reuptake transporter expression in irritable bowel syndrome is modulated by gut microbiota via mast cell-prostaglandin E2. *Gastroenterology* **162**, 1962–1974.e1966 (2022).
22. Barbara, G. et al. Mast cell-dependent excitation of visceral-nociceptive sensory neurons in irritable bowel syndrome. *Gastroenterology* **132**, 26–37 (2007).
23. Ross, J. A. & Kasum, C. M. Dietary flavonoids: bioavailability, metabolic effects, and safety. *Annu. Rev. Nutr.* **22**, 19–34 (2002).
24. Collins, S. M. A role for the gut microbiota in IBS. *Nat. Rev. Gastroenterol. Hepatol.* **11**, 497–505 (2014).
25. Zhong, D. et al. Orally deliverable strategy based on microalgal biomass for intestinal disease treatment. *Sci. Adv.* **7**, eabi9265 (2021).
26. Zhang, D. et al. Microalgae-based oral microcarriers for gut microbiota homeostasis and intestinal protection in cancer radiotherapy. *Nat. Commun.* **13**, 1413 (2022).
27. Soni, R. A., Sudhakar, K. & Rana, R. S. Spirulina – From growth to nutritional product: A review. *TRENDS FOOD Sci. Tech.* **69**, 157–171 (2017).
28. Torres-Tijji, Y., Fields, F. J. & Mayfield, S. P. Microalgae as a future food source. *Biotechnol. Adv.* **41**, 107536 (2020).
29. Wu, Q. et al. The antioxidant, immunomodulatory, and anti-inflammatory activities of Spirulina: an overview. *Arch. Toxicol.* **90**, 1817–1840 (2016).
30. Yu, T. et al. Spirulina platensis alleviates chronic inflammation with modulation of gut microbiota and intestinal permeability in rats fed a high-fat diet. *J. Cell. Mol. Med.* **24**, 8603–8613 (2020).
31. Huang, S.-T. et al. Glutamatergic and GABAergic anterodorsal BNST projections to PVN CRH neurons regulate maternal separation-induced visceral pain. *Neuropsychopharmacology* **48**, 1778–1788 (2023).
32. Mercer Lindsay, N., Chen, C., Gilam, G., Mackey, S. & Scherrer, G. Brain circuits for pain and its treatment. *Sci. Transl. Med.* **13**, eabj7360 (2021).
33. Farasati Far, B. et al. Enhanced antibacterial activity of porous chitosan-based hydrogels crosslinked with gelatin and metal ions. *Sci. Rep.* **14**, 7505 (2024).
34. Bertiaux-Vandaële, N. et al. The expression and the cellular distribution of the tight junction proteins are altered in irritable bowel syndrome patients with differences according to the disease subtype. *Am. J. Gastroenterol.* **106**, 2165–2173 (2011).
35. Gustafsson, J. K. & Johansson, M. E. V. The role of goblet cells and mucus in intestinal homeostasis. *Nat. Rev. Gastroenterol. Hepatol.* **19**, 785–803 (2022).
36. Aguilera-Lizarraga, J. et al. Local immune response to food antigens drives meal-induced abdominal pain. *Nature* **590**, 151–156 (2021).
37. Nie, X. et al. The innate immune receptors TLR2/4 mediate repeated social defeat stress-induced social avoidance through prefrontal microglial activation. *Neuron* **99**, 464–479.e467 (2018).
38. Meynier, M. et al. Pasteurized Akkermansia muciniphila improves irritable bowel syndrome-like symptoms and related behavioral disorders in mice. *Gut Microbes* **16**, 2298026 (2024).
39. Liu, X. et al. Blautia—a new functional genus with potential probiotic properties?. *Gut Microbes* **13**, 1–21 (2021).
40. Ford, A. C., Vanner, S., Kashyap, P. C. & Nasser, Y. Chronic visceral pain: new peripheral mechanistic insights and resulting treatments. *Gastroenterology* **166**, 976–994 (2024).
41. Bayrer, J. R. et al. Gut enterochromaffin cells drive visceral pain and anxiety. *Nature* **616**, 137–142 (2023).
42. Waclawiková, B., Codutti, A., Alim, K. & El Aidy, S. Gut microbiota-motility interregulation: insights from in vivo, ex vivo and in silico studies. *Gut Microbes* **14**, 1997296 (2022).
43. Wang, P. et al. Sodium butyrate triggers a functional elongation of microglial process via Akt-small RhoGTPase activation and HDACs inhibition. *Neurobiol. Dis.* **111**, 12–25 (2018).
44. Dalile, B., Van Oudenhove, L., Vervliet, B. & Verbeke, K. The role of short-chain fatty acids in microbiota–gut–brain communication. *Nat. Rev. Gastroenterol. Hepatol.* **16**, 461–478 (2019).
45. Effinger, A., O’Driscoll, C. M., McAllister, M. & Fotaki, N. Impact of gastrointestinal disease states on oral drug absorption - implications for formulation design - a PEARL review. *J. Pharm. Pharmacol.* **71**, 674–698 (2019).
46. Ford, A. C., Lacy, B. E. & Talley, N. J. Irritable bowel syndrome. *N. Engl. J. Med.* **376**, 2566–2578 (2017).
47. Howell, C. A. et al. Double-blinded randomised placebo controlled trial of enterogel (polymethylsiloxane polyhydrate)

- for the treatment of IBS with diarrhoea (IBS-D). *Gut* **71**, 2430–2438 (2022).
48. Ibeakanma, C. et al. Brain-gut interactions increase peripheral nociceptive signaling in mice with postinfectious irritable bowel syndrome. *Gastroenterology* **141**, 2098–2108.e2095 (2011).
 49. Collins, J. W. et al. *Citrobacter rodentium*: infection, inflammation and the microbiota. *Nat. Rev. Microbiol.* **12**, 612–623 (2014).
 50. Mullineaux-Sanders, C. et al. *Citrobacter rodentium*-host-microbiota interactions: immunity, bioenergetics and metabolism. *Nat. Rev. Microbiol.* **17**, 701–715 (2019).
 51. Lembo, A. et al. Repeat treatment with rifaximin is safe and effective in patients with diarrhea-predominant irritable bowel syndrome. *Gastroenterology* **151**, 1113–1121 (2016).
 52. Zhang, D. et al. Short-chain fatty acids in diseases. *Cell Commun. Signal.* **21**, 212 (2023).
 53. Liu, J.-S. et al. Natural product myricetin is a pan-KDM4 inhibitor which with poly lactic-co-glycolic acid formulation effectively targets castration-resistant prostate cancer. *J. Biomed. Sci.* **29**, 29 (2022).
 54. Marasco, G., Savarino, E. V. & Barbara, G. The IBS and SIBO dilemma: here we go again. *Digestive Liver Dis.* **56**, 2025–2026 (2024).
 55. Alsaikhan, F. & Farhood, B. Recent advances on chitosan/hyaluronic acid-based stimuli-responsive hydrogels and composites for cancer treatment: a comprehensive review. *Int. J. Biol. Macromol.* **280**, 135893 (2024).
 56. Marles, R. J. et al. United States pharmacopeia safety evaluation of spirulina. *Crit. Rev. Food Sci. Nutr.* **51**, 593–604 (2011).

Acknowledgements

This work was supported by the National Key R&D Program of China (2022YFA1104900, M.Z.), the Natural Science and Foundation of Shandong Province (ZR2023ZD30, M.Z.), the Binjiang Institute of Zhejiang University (ZY202205SMKY007, M.Z.), the Medical Science and Technology Project of Zhejiang Province (2022RC024, M.Z.). We thank Liu Di from the Core Facilities, The Zhejiang University-University of Edinburgh Institute, Zhejiang University for her technical support, Tan Haiming from the Laboratory Animal Center of the International Campus of Zhejiang University for his technical support and Lin Zhaoxiaonan and Shuangshuang Liu from the core facilities Zhejiang university school of medicine for her technical support. Allen brain map, Figdraw, Scidraw.io, BioRender and TogoTV were used in the drawing of some schematic diagrams.

Author contributions

M.Z. conceived the project. J.Y., H.S., Q.Z. and J.H. performed the experiments. J.Y. and H.S. analyzed and interpreted the data. J.Y. wrote the original draft. M.Z. reviewed and edited the manuscript.

Competing interests

The authors declare no competing interests.

Additional information

Supplementary information The online version contains supplementary material available at <https://doi.org/10.1038/s41467-025-62360-2>.

Correspondence and requests for materials should be addressed to Min Zhou.

Peer review information *Nature Communications* thanks the anonymous reviewers for their contribution to the peer review of this work. A peer review file is available.

Reprints and permissions information is available at <http://www.nature.com/reprints>

Publisher's note Springer Nature remains neutral with regard to jurisdictional claims in published maps and institutional affiliations.

Open Access This article is licensed under a Creative Commons Attribution-NonCommercial-NoDerivatives 4.0 International License, which permits any non-commercial use, sharing, distribution and reproduction in any medium or format, as long as you give appropriate credit to the original author(s) and the source, provide a link to the Creative Commons licence, and indicate if you modified the licensed material. You do not have permission under this licence to share adapted material derived from this article or parts of it. The images or other third party material in this article are included in the article's Creative Commons licence, unless indicated otherwise in a credit line to the material. If material is not included in the article's Creative Commons licence and your intended use is not permitted by statutory regulation or exceeds the permitted use, you will need to obtain permission directly from the copyright holder. To view a copy of this licence, visit <http://creativecommons.org/licenses/by-nc-nd/4.0/>.

© The Author(s) 2025